

Department of the Environment, Transport, Energy and Communication DETEC Swiss Federal Office of Energy SFOE Energy Research

## **DURAPEM**

On the use of supported and high surface area Ir-oxides as O<sub>2</sub>-evolution (co-)catalysts for water electrolyzers and starvation events in fuel cells



Date: 04 December 2020

Place: Bern

#### Publisher:

Swiss Federal Office of Energy SFOE Research Programme Hydrogen CH-3003 Bern www.bfe.admin.ch energieforschung@bfe.admin.ch

#### Co-financed by:

Umicore AG & Co KG Rodenbacher Chaussee 4 63457 Hanau, Deutschland

#### Authors:

Natasa Diklic, Adrian Heinritz, Alexandra Patru, Juan Herranz, Thomas J. Schmidt – Electrochemistry Laboratory, Paul Scherrer Institut

**SFOE head of domain:** Stefan Oberholzer, <u>stefan.oberholzer@bfe.admin.ch</u> **SFOE programme manager:** Stefan Oberholzer, <u>stefan.oberholzer@bfe.admin.ch</u>

SFOE contract number: SI/501602-01

The author of this report bears the entire responsibility for the content and for the conclusions drawn therefrom.



## **Summary**

The conversion of intermittent, renewable energy into storable hydrogen through water electrolysis and the subsequent re-electrification of this H<sub>2</sub> in polymer electrolyte fuel cells constitutes one of the most appealing pathways for the development of an environmentally benign energy scenario. Nevertheless, the realization of this archetype requires improvements in the production-/operative-costs and durability of these energy conversion devices. For electrolyzers, these issues are largely related to the anodic oxygen evolution reaction (OER), which constitutes the main contributor to their efficiency losses and is catalysed using scarce iridium oxides that contribute significantly to their production costs. In the case of fuel cells, their operation can entail momentary interruptions in the H<sub>2</sub>-supply (i.e., so called *starvation* events) that lead to high potentials at which the carbon support used in the Pt-based, hydrogen-oxidation anode catalyst gets corroded, severely jeopardizing the performance of this component. This is often avoided by including in the anode catalyst layer the same kind of Ir-based catalysts discussed above, which promote the OER over the corrosion of carbon and, in doing so, prevent anode degradation.

Based on these two key applications, the development of highly active and stable iridium oxide (IrO<sub>x</sub>) OER-catalysts can be regarded as a cornerstone for the commercial success of electrolyzers and fuel cells. This passes by developing approaches to increase these materials' dispersion, which can tentatively be done by using a support. Thus, in the first part of this project, we characterized and electrochemically tested several IrO<sub>x</sub> catalysts provided by Umicore AG and that in some cases had been prepared using Nb<sub>2</sub>O<sub>5</sub> as a support. Our electrochemical results unveil a direct correlation between these materials' surface area and their initial OER-activity, along with an improvement of the durability of the supported catalysts for which the precise mechanisms were exhaustively investigated.

Subsequently, in the second part of the project the same kind or materials were tested as  $H_2$ -starvation co-catalysts in fuel cell anodes. Our results in this regard unveil the importance of water management on the success of this approach, which had been overlooked in previous studies on the matter and puts into question the validity of the control tests customarily used to study such starvation events. Most importantly, our experiments also allowed us to prove for the first time that this starvation events can become irreversible for anodes implementing the ultra-low Pt-loadings (< 50  $\mu$ gPt-cm<sup>-2</sup>) that the fuel cell sector is striving to achieve (as to decrease manufacturing costs).

Finally, in the third part of this report, we present our results regarding two in-house produced, high surface area iridium oxides displaying different compositions (i.e., IrOOH vs. IrO<sub>2</sub>) and concomitant OER-activities and durabilities. Specifically, whereas the higher surface area IrOOH was more OER active than rutile IrO<sub>2</sub>, the opposite trend was observed regarding the materials' durability. This last effect was subsequently studied using a setup that allows combining X-ray absorption spectroscopy (XAS) and small angle X-ray scattering (SAXS), as to simultaneously asses the operando changes in the samples' composition and morphology. Chiefly, while the catalysts' oxidation state and coordination environment did not change in the curse of the stability tests (as inferred from XAS), the morphology of the IrOOH sample underwent significant changes that led to its agglomeration and the concomitant loss of activity observed in these experiments.





## **Contents**

Summ	nary	3
Conte	ents	5
List of	f abbreviations	6
Part 1	Commercial iridium oxide catalysts for O <sub>2</sub> -evolution in polymer electrolyte was electrolyzers	er
1.1	Introduction	7
1.2	Experimental section	8
1.3	Results and Discussion	10
1.3.1	Structural characterization	10
1.3.2	Electrochemical characterization and OER-activity	13
1.4	Conclusions and outlook	21
1.3	References	22
Part 2	2 Commercial iridium oxide catalysts for H <sub>2</sub> -starvation in polymer electrolyte fue anodes	el cell
2.1	Introduction	25
2.2	Experimental section	25
2.3	Results and discussion	26
2.3.1	Water management	26
2.3.2	Reversal trapped state	28
2.4	Conclusions and outlook	28
2.5	References	29
Part 3	s Combining SAXS and XAS to study <i>in-house</i> , high surface area iridium oxides	i.
3.1	Introduction	30
3.2	Experimental section	30
3.3	Results and discussion	32
3.3.1	Materials' characterization and electrochemical behaviour	32
3.3.2	Operando compositional changes assessed by XAS	
3.3.3	SAXS-derived operando changes in the oxides' morphology	34
3.4	Conclusions and outlook	35
3.5	References	36



## List of abbreviations

AST Accelerated stress test

CCM Catalyst coated membrane

EXAFS Extended X-ray absorption fine structure

IL Identical location

MEA Membrane electrode assembly

OER Oxygen evolution reaction

PEFC Polymer electrolyte fuel cell

PEM Proton exchange membrane

PEWE Polymer electrolyte water electrolyzer

RDE Rotating disc electrode

RHE Reversible hydrogen electrode

SA Surface area

SAXS Small angle X-ray scattering

SEM Scanning electrode microscopy

SLS Swiss light source

TEM Transmission electron microscopy

XANES X-ray absorption near-edge structure

XAS X-ray absorption spectroscopy



# Part 1.- Commercial iridium oxide catalysts for O<sub>2</sub>-evolution in polymer electrolyte water electrolyzers

#### 1.1 Introduction

To assure the energetic transition from fossil fuels to more environmentally friendly energy resources, many efforts are being directed towards the development of efficient and cost competitive energy storage and conversion technologies. In this context, hydrogen is broadly regarded as a key energy carrier (e.g., for its re-electrification in (automotive) fuel cells, or as a feedstock for the chemistry sector), but its environmentally benign production relies on the continued development of polymer electrolyte water electrolyzers (PEWEs). To reach the H<sub>2</sub>-production costs needed to render this technology cost-competitive (< 2 US\$/kgH<sub>2</sub>), further improvements in the operative efficiency and device costs of PEWEs are urgently needed. Interestingly, both of these requirements are linked to the oxidation evolution reaction (OER) taking place in PEWE anodes, since it constitutes the main source of operative efficiency losses and the costly iridium oxides (IrO<sub>x</sub>) used to catalyze it represents a major contributor to the devices' cost. Thus, ongoing research efforts focus on the development of IrO<sub>x</sub>-catalysts with enhanced OER-activities allowing a decrease of the amount of metal in each device and of the efficiency losses associated to this reaction.

One approach to increase this OER-activity is to use supports that enhance the dispersion of the catalyst (i.e., the fraction of its surface available for the reaction) and can therefore allow a reduction of the quantity of precious metal. To evaluate potential candidates for such a support task, Han et al. [1] screened for oxides are electrochemically stable at OER conditions (i.e., potentials ≤ 2 V versus the reversible hydrogen electrode (VRHE)) and at pH 0. According their Pourbaix diagram, they predicted the sufficient stability for MoO<sub>3</sub>, RuO<sub>2</sub>, Sb<sub>2</sub>O<sub>5</sub>, TeO<sub>3</sub>, WO<sub>3</sub>, OsO<sub>4</sub>, PtO<sub>2</sub>, IrO<sub>2</sub>, Nb<sub>2</sub>O<sub>5</sub>, ZrO<sub>2</sub>, Ta<sub>2</sub>O<sub>5</sub> and HfO<sub>2</sub>, and potentially also for TiO2, MnO2, Cu2O3, GeO2, AgO, SnO2, Tl2O3, PbO2 and Bi4O7. Interestingly, while supports with electronic conductivities < 1 S·cm<sup>-1</sup> may be considered unsuitable for this task, numerous studies have reported a positive impact of the use of such electrically inert supports on the stability of IrO2- or RuO2-based catalysts, without compromising the OER-activity and leading to a concomitant decrease of the catalyst costs [2-5]. Moreover, there are variety of synthesis methods that allow tuning the catalyst architecture as to produce an electrically percolating structure in which the inert oxide support is uniformly covered by a continuous shell of the conductive IrOx. Examples of such coreshell catalysts include IrO<sub>2</sub>@TiO<sub>2</sub>, which was shown to outperformed many catalysts that were focused on the use of conductive support [6], un-doped SnO<sub>2</sub> [7] and other commercially available Ir-catalysts supported on nonconductive support such as TiO<sub>2</sub> and Ta<sub>2</sub>O<sub>5</sub>. [8–10].

Among the various oxide supports discussed above,  $Nb_2O_5$  has been reported to have a positive effect on the OER performance of  $IrO_2$  [2], but only a few studies have investigated in greater detail such  $IrO_2/Nb_2O_5$  catalysts. While Terezo et al. [11] examined the influence of synthesis parameters on  $IrO_2/Nb_2O_5$  OER activity and stability, Zlotorowicz et al. [12] found that the presence of  $Nb_2O_5$  plays a beneficial role at high temperatures. Here we present a detailed investigation of the influence of the Nb-precursor used in synthesis of several commercial  $IrO_2/Nb_2O_5$  catalysts provided by Umicore AG on their OER-activity and stability. In addition, potential artifacts related to the rotating disk electrode (RDE) technique commonly used to assess these materials' electrochemical performance and durability are discussed in detail.



## 1.2 Experimental Section

*Materials.*– The catalysts evaluated in this study include pure IrO₂ as well as IrO₂/Nb₂O₅ mixed oxides. All catalysts (IrO₂ MA 1023 A2, IrNbOx BRO 0471 A1 and IrNbOx MA 1001 A1) were provided by Umicore®. The mixed oxides contain ≈ 75 wt % Ir and they differ in the precursor used in their synthesis; namely, IrO₂ MA 1023 A2 and IrNbOx BRO 0471 A1 were synthesized using an acetate-based (Ac) precursor, while for the synthesis of IrNbOx MA 1001 A1 a chlorine precursor (CI) was used. In what follows all catalysts appear labeled according to the precursor used, i.e., as IrO₂ (Ac), IrO₂/Nb₂O₅ (Ac) or IrO₂/Nb₂O₅ (CI).

Electrochemical characterization.— For the RDE measurements, catalyst inks were prepared dispersing 10 mg of the catalyst of choice in 4 mL of isopropyl alcohol (HPLC Plus, Sigma Aldrich), 1 mL of ultrapure water (18.2 MΩ·cm, ELGA Purelab) and 20 μL of Nafion solution (≈ 5 wt% Nafion® perfluorinated resin solution). The ink suspensions were sonicated for 30 min before depositing on a glassy carbon (SIGRADUR® G, HTW Hochtemperatur-Werkstoffe GmbH) embedded in polytetrafluoroethylene (PTFE) RDE (Pine Research). The working electrode was prepared using a spin coating method. 5 μL of the ink was dropped on the inverted electrode at a rotating speed of 60 rpm, followed by a gradual increase of the speed up to 500 rpm. A graduated cylinder was used to protect the electrode from contamination while drying. The deposition process was repeated twice, yielding a catalyst loading of ≈ 100 μg<sub>cat</sub>·cm-².

The OER activity and stability evaluation of the various IrO<sub>2</sub> based catalysts presented in this study were performed in a glass three-electrode cell. The glassware had been previously cleaned in a 3:1 mixture of 98 % H<sub>2</sub>SO<sub>4</sub> and 30 % H<sub>2</sub>O<sub>2</sub> overnight, and boiled in ultrapure water at least three times prior to the measurements. All measurements were performed at room temperature, using 0.1 M HCIO4 electrolyte (made from KANTO Chemical CO. or VERITAS double distilled concentrated acid) saturated with synthetic air. A mercury/mercurous sulfate electrode pre-calibrated against the reversible hydrogen electrode in the same electrolyte and a gold mesh were used as reference and counter electrodes, respectively. To evaluate the catalyst's OER activity, polarization curves were derived from chronoamperometric measurements in which the potential was gradually stepped from 1.2 to 1.56 V<sub>RHE</sub> while holding for 1 min at each potential. The current value plotted in these polarization curves corresponds to the last point in each of these potential steps. Electrochemical impedance spectroscopy measurements were recorded at 1 V<sub>RHE</sub> in a frequency range from 200 kHz to 1 Hz with an amplitude of 10 mV. The high frequency resistance was used for the ohmic drop correction of the polarization curves. Additionally, cyclic voltammograms (CVs) were recorded before and after the polarization curve measurements in order to evaluate potential surface changes. These CV measurements were performed between 1.0 and 1.4 V<sub>RHE</sub> at 50 and 10 mV·s<sup>-1</sup>. The materials' stability was examined via an accelerated stress test (AST) consisting of 10 s potential holds at 1 and 1.6 V<sub>RHE</sub>. The current is normalized with regards to the beginning-of-test value based on the last point at 1.6 VRHE after every 100 cycles. Additionally, CVs and impedance spectra were also recorded every 100 cycles. For the activity measurement, the electrode rotation was set to 1600 rpm, while 2900 rpm was required for the longer stability measurements to efficiently remove formed O<sub>2</sub> bubbles.

A flow cell setup described elsewhere [13] was used to examine changes in the catalysts' crystallinity, morphology and surface oxidation state via *operando* X-ray diffraction, *post mortem* transmission electron microscopy and X-ray photoelectron spectroscopy, respectively (see below for more information on these techniques).



Physicochemical characterization.— The electrical conductivity of the materials was assessed by four-wire impedance spectroscopy measurements. The pressed powders were kept under a constant pressure of 0.6 MPa at room temperature for a few minutes before the measurements. Impendence spectroscopy was performed applying a 2 to 5 mV amplitude perturbation in frequency range between 1 MHz and 1 Hz. Nitrogen adsorption/desorption experiments were performed to determine the surface area of the materials, which was derived from the Brunauer–Emmett–Teller (BET) equation of N<sub>2</sub>-sorption isotherms (Autosorb-1, Quantachrome Instruments, Boynton Beach, FL, USA).

X-ray diffraction (XRD) measurements were performed using a Smart Lab Rigaku system equipped with a copper rotating anode as the X-ray source. The diffraction patterns were recorded in Bragg Brentano geometry (Θ/2Θ), with the source operating at 160 mA and 40 kV. A Kβ filter was used to remove copper-Kβ radiation. Information about the chemical state of Ir, Nb and O at the surface was obtained by X-ray photoelectron spectroscopy (XPS). These measurements were performed using a VG ESCALAB 220iXL spectrometer operating with a monochromatic Al Kα source (15 kV / 150 W). Charging effects were corrected by setting the binding energy of the C 1s peak maximum to an energy of 284.8 eV. The analysis of the spectra was carried out using Casa XPS software [14]. Background subtraction was performed according to Shirley [15] while Scofield atomic sensitivity factors [16] and transmission corrections were applied for proper atomic quantification. Doniach-Sunjić (DS) and Gaussian Lorenzian sum (SGL) functions were employed to fit the Ir 4f peak, together with Gaussian/Lorenzian (GL) product functions used for its satellites, as described in reference [17]. The final line shape was determined from a rutile IrO2 reference sample provided by Umicore®. For the Nb 3d line, a GL(30) function was used, while the O 1s peak required different line shapes for IrO<sub>2</sub> and Nb<sub>2</sub>O<sub>5</sub>. Namely, O 1s arising from the IrO<sub>2</sub> lattice requires an asymmetric peak shape, since the same conduction electron states screen O 1s and Ir 4f holes [18,19], while the O 1s line shape associated with Nb₂O₅, OH and H₂O contribution was set to the GL(30) line shape.

The morphology of the catalysts was investigated using transmission electron microscopy (TEM) and scanning electron microscopy (SEM). TEM images were acquired in a TECNAI F30 operated at 300 kV, and SEM measurements were performed in a Carl Zeiss Ultra55 microscope, using the in-lens detector at an acceleration voltage of 3 to 5 kV. For identical location (IL-) SEM studies, a strip of copper tape was placed over the RDE as to contact a small part of the catalyst-loaded disk and the sample holder, thus reducing charging issues. In order to quantify dissolved species during the AST, a miniature glass cell requiring 9 mL of electrolyte was employed in order to decrease the ratio between volume of electrolyte and catalyst mass. Traces of dissolved Ir and Nb cationic species were quantified by inductively coupled plasma optical emission spectrometry (ICP-OES) using an Agilent 7700x station.

Quick acquisition X-ray absorption spectroscopy (Q-XAS) measurements were performed at the SuperXAS beamline of the Swiss Light Source (SLS - Villigen PSI, Switzerland). Structural characterization was performed within an energy range corresponding to the Ir L<sub>3</sub> (11,215 eV) or Nb K edges (18,986 eV). Nb<sub>2</sub>O<sub>5</sub> (Sigma Aldrich) and NbO<sub>2</sub> (Chemie Brunschwig AG) were employed as references for Nb<sup>5+</sup> and Nb<sup>4+</sup> oxidation states. All samples were pressed into pellets with cellulose as a dilutant. The beamline energy was calibrated with Pt, Mo and Nb reference foils to the Pt L<sub>3</sub> edge position at 11,564 eV, Mo K edge at 20,000 eV and Nb K at 18,986 eV.

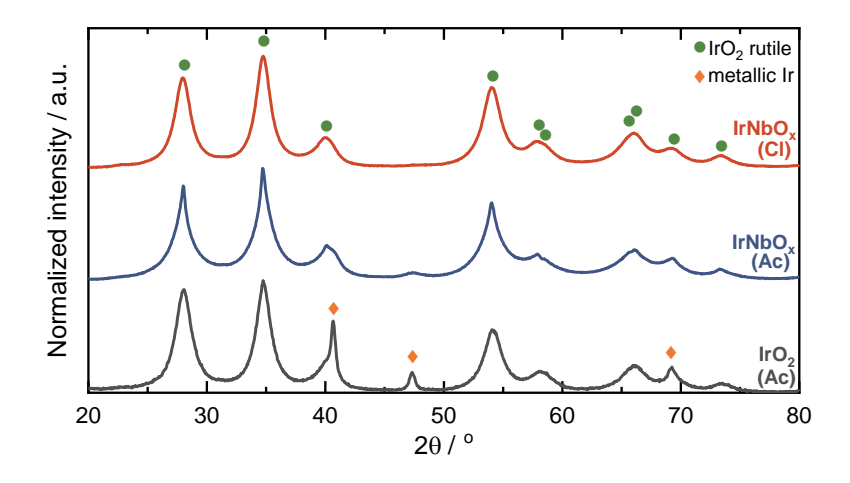
Using the ProQEXAFS software [20], 59 spectra acquired within 1 min were averaged and energy-calibrated. Further processing such as background substraction and edge step normalization was done using the Demeter software package [21].  $E_0$  was determined as a the maximum of the spectral first derivative. The extended X-ray absorption fine structure (EXAFS) spectra were obtained by performing a Fourier transform over a k range of 3 to 15 Å<sup>-1</sup>. The spectra were k<sup>3</sup>-weighted in order to compensate for dampening of the amplitude at higher k-values. The theoretical model used for EXAFS fitting of Ir spectra was generated from  $IrO_2$  rutile structure (card 81028 ICSD). The EXAFS data was fitted over a 1.1 – 4.0 Å window.



## 1.3 Results and discussion

#### 1.3.1 Structural characterization

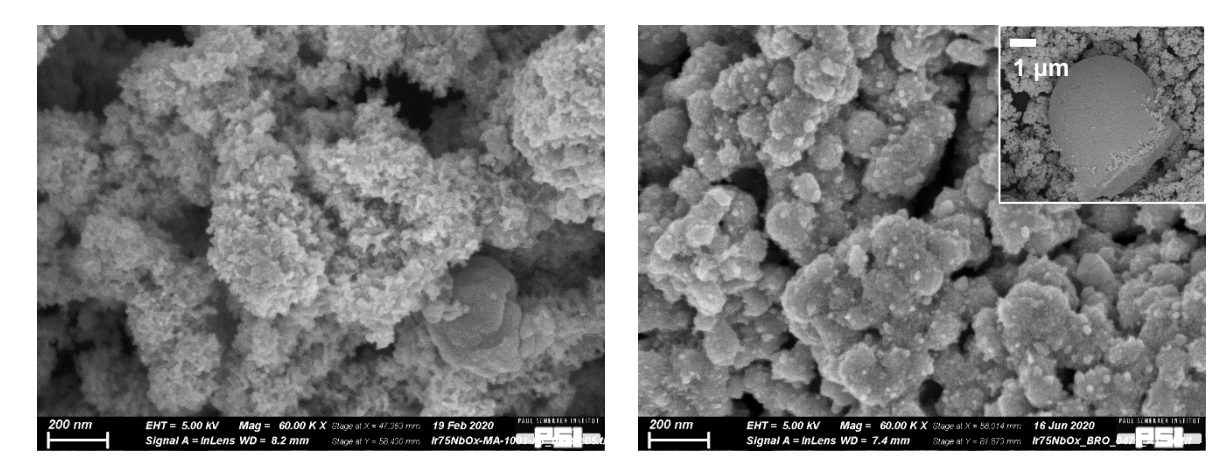
Although Nb<sub>2</sub>O<sub>5</sub> is known to be an insulating material, [22,23] the electrical conductivity of the IrO<sub>2</sub>/Nb<sub>2</sub>O<sub>5</sub> catalyst showed just a minor decrease compared to the unsupported, pure IrO<sub>2</sub>. More precisely, IrO<sub>2</sub>/Nb<sub>2</sub>O<sub>5</sub> (Ac) and (CI) exhibited conductivity values of 7 ± 2 and 6.4 ± 0.3 S·cm<sup>-1</sup>, respectively, while the conductivity of IrO<sub>2</sub> was 11.8 ± 0.6 S·cm<sup>-1</sup>. Moving on, Figure 1.1 shows a comparison of the XRD patterns of those same three materials. IrO<sub>2</sub>/Nb<sub>2</sub>O<sub>5</sub> (CI) features diffraction peaks typical for the IrO<sub>2</sub> rutile phase (ICSD code 81028), while pure IrO<sub>2</sub> (Ac) and IrO<sub>2</sub>/Nb<sub>2</sub>O<sub>5</sub> (Ac) contain residual traces of metallic Ir (ICSD code 64992). Moreover, no peaks related to Nb<sub>2</sub>O<sub>5</sub> are present on any of XRD patterns, which can be due to its small content or because of this Nb-oxide being present in an amorphous, hydrous form. The additional lack of shifts in the diffraction peaks of IrO<sub>2</sub> indicate a lack of segregation between the IrO<sub>2</sub> and Nb<sub>2</sub>O<sub>5</sub> phases, and the resembling full widths at half maximum all materials' diffraction peaks indicate that they all feature similar crystallite sizes.



**Figure 1.1.** XRD patterns of IrO<sub>2</sub>/Nb<sub>2</sub>O<sub>5</sub> (CI), IrO<sub>2</sub>/Nb<sub>2</sub>O<sub>5</sub> (Ac) and pure IrO<sub>2</sub> (Ac), including the diffraction positions expected for rutile IrO<sub>2</sub> and metallic Ir references.

Next, the SEM images in Figure 1.2 illustrate the difference in morphology between these catalysts. Specifically, while  $IrO_2/Nb_2O_5$  (CI) consists of needle-like aggregates,  $IrO_2/Nb_2O_5$  (Ac) features more compact particles. This morphological difference is in line with their BET surface area, which is  $\approx$  2-fold higher for  $IrO_2/Nb_2O_5$  (CI) (24  $m^2g^{-1}$ ) vs.  $IrO_2/Nb_2O_5$  (Ac) (9  $m^2g^{-1}$ ). Note that the BET surface area of  $IrO_2$  (Ac) was 5  $m^2g^{-1}$ . According to energy dispersive X-ray spectroscopy (EDX) results acquired at different spots across the catalysts,  $IrO_2/Nb_2O_5$  (CI) displays a uniform distribution of Ir and Nb, with an Ir/Nb weight ratio  $\approx$  12.1  $\pm$  0.2, while in the case of  $IrO_2/Nb_2O_5$  (Ac) the material features a relatively inhomogeneous distribution of Ir and Nb, with an Ir/Nb weight ratio was 25  $\pm$  4. This higher Ir/Nb ratio is not related to a higher Ir content compared with  $IrO_2/Nb_2O_5$  (CI), but to the fact that  $Nb_2O_5$  is not uniformly distributed and forms agglomerates, as pointed out in Figure 1.2b.

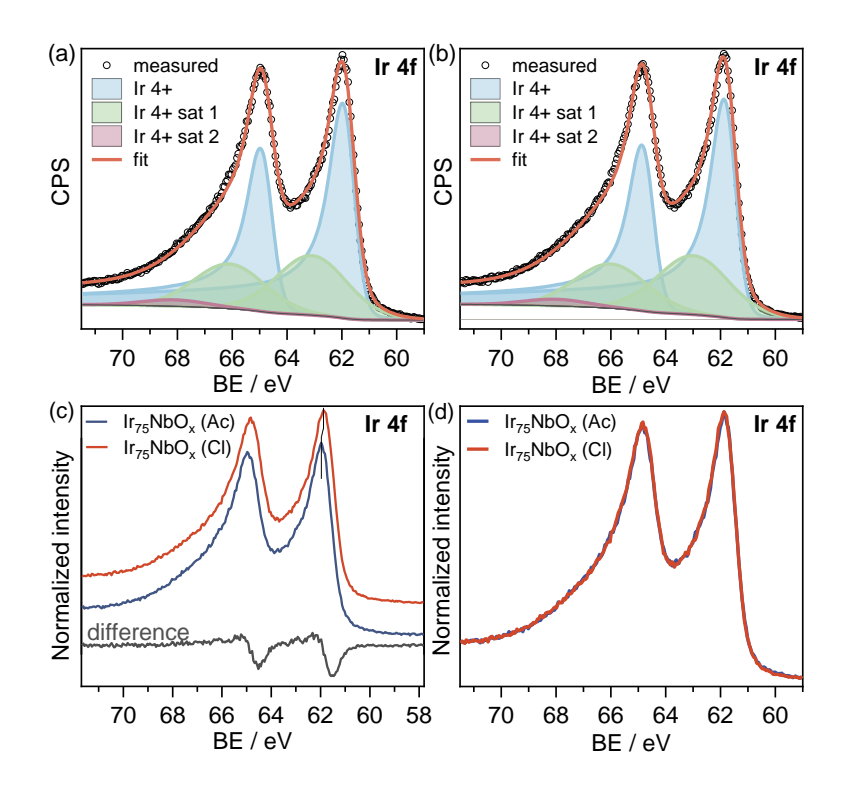




**Figure 1.2.** SEM images of IrO<sub>2</sub>/Nb<sub>2</sub>O<sub>5</sub> (CI) (a) and IrO<sub>2</sub>/Nb<sub>2</sub>O<sub>5</sub> (Ac) (b), in the latter case including an inset that shows the inhomogeneous distribution of the Nb<sub>2</sub>O<sub>5</sub> in this material.

The surface oxidation state of both as-synthesized catalysts was evaluated using XPS. As shown in Figure 1.3, the Ir 4f peak in  $IrO_2/Nb_2O_5$  (Ac) is shifted by  $\approx 0.1$  eV towards higher binding energies compared to  $IrO_2/Nb_2O_5$  (CI), which would indicate the presence of reduced Ir species in  $IrO_2/Nb_2O_5$  (Ac) [17]. Considering the XRD results discussed above, though, one would expect an energy shift in the opposite direction, since  $IrO_2/Nb_2O_5$  (Ac) contains metallic Ir. Additionally, the presence of Ir species in such a different oxidation state would lead to a distortion of Ir 4f doublet. However, if the Ir 4f peaks of the two samples are aligned (see Figure 1.3d), no difference in their peak shapes can be observed. This suggests that the Ir in both catalysts is in the same oxidation state, and that the slight binding energy shift discussed above may be caused by imprecisions in the calibration of spectra, which relies on the binding energy of adventitious C 1s peak (*vide supra*) that is reported to be imprecise due to the unknown composition of the carbon contributing to this signal [24]. Finally, peak deconvolution shows that Ir is in a 4+ oxidation state and that no metallic Ir is present on the catalysts' surface.

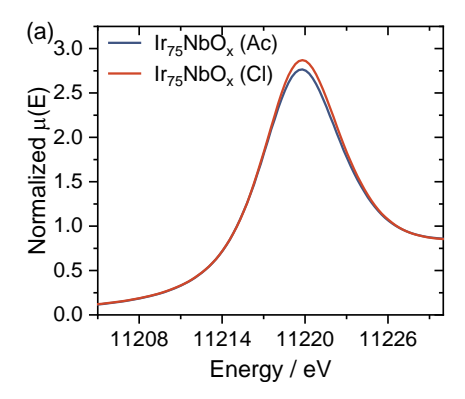




**Figure 1.3.** Deconvoluted Ir 4f XPS spectra of  $IrO_2/Nb_2O_5$  (Ac) (a) and  $IrO_2/Nb_2O_5$  (Cl) (b), along with the comparison and difference of those two (c) and their overlay after alignment of the spectral maxima to the same binding energy.

To further investigate the local electronic and atomic structure of these materials, they were characterized by means of XAS. According to the X-ray absorption near edge structure (XANES) spectra, IrO<sub>2</sub>/Nb<sub>2</sub>O<sub>5</sub> (CI) exhibits a higher intensity of the white line (Figure 1.4a) representative of transitions from 2p<sub>3/2</sub> level to unoccupied 5d states near the Fermi level [25]. Therefore, the higher the intensity of the white line originate from higher probability of electron transition from 2p<sub>3/2</sub> to 5d state. Thus higher density of unoccupied 5d states is present in the case of IrO2/Nb2O5 (CI), meaning that this material is more oxidized compared to IrO<sub>2</sub>/Nb<sub>2</sub>O<sub>5</sub> (Ac). This is in line with the XRD results presented above, which showed that IrO<sub>2</sub>/Nb<sub>2</sub>O<sub>5</sub> (Ac) contains a small contribution of metallic Ir. On the other hand, XAS is a technique that (unlike XRD) is sensitive to the local structure of amorphous samples. Therefore, XAS at Nb edge was also acquired as well to gain complementary information about this Nb<sub>2</sub>O<sub>5</sub> support, which displayed no diffraction peaks in the XR-diffractograms discussed above. As shown in Figure 1.4b, the XANES spectra at the Nb edge is the same for both materials, are shifted towards higher energies compared to the reference spectra for Nb4+ and exhibit a pre-edge feature specific to Nb5+, if not fully resembling the spectrum of Nb₂O₅. The K edge of Nb exhibits a higher spetrcal maximum at ≈ 19,012 eV that is not specific to Nb<sub>2</sub>O<sub>5</sub>, but to niobic acid [26], suggesting that the Nb<sub>2</sub>O<sub>5</sub> reference is most likely present in this hydrated state. Complementarily, the Ir L<sub>3</sub> EXAFS spectra revealed no significant difference among samples, with both IrO<sub>2</sub>/Nb<sub>2</sub>O<sub>5</sub> (CI) and IrO<sub>2</sub>/Nb<sub>2</sub>O<sub>5</sub> (Ac) displaying similar Ir-O bonding distances (1.980 vs. 1.987 Å, respectively) typical for rutile type IrO2 [27]. Additionally, this can confirm no segregation effects with Nb<sub>2</sub>O<sub>5</sub>.





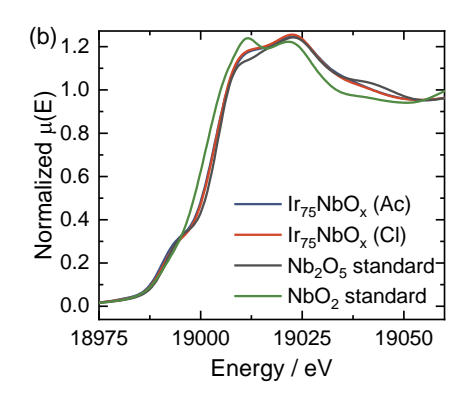


**Figure 1.4.** Ir L<sub>3</sub> XANES spectra of IrO<sub>2</sub>/Nb<sub>2</sub>O<sub>5</sub> (Ac) and IrO<sub>2</sub>/Nb<sub>2</sub>O<sub>5</sub> (Cl) (b) and the corresponding spectra of the same samples (including Nb<sup>4+</sup> and Nb<sup>5+</sup> references) at the Nb K edge.

#### 1.3.2 Electrochemical characterization and OER-activity

In a first stage, the catalysts were characterized by cyclic voltammetry, for which the results are shown in Figure 1.5. The  $IrO_2/Nb_2O_5$  (CI) sample features a larger double layer capacitance than  $IrO_2/Nb_2O_5$  (Ac), in agreement with its  $\approx$  2-fold greater BET surface area (*vide supra*). Notably, the current peaks appearing at  $\approx$  0.8  $V_{RHE}$  in the CV of  $IrO_2/Nb_2O_5$  CI indicate an Ir 3+/4+ redox transition [17], and suggest submonolayer coverages of Ir 3+ species on the catalyst surface that could not be inferred from the XPS results presented above. Comparatively, the CV of the  $IrO_2/Nb_2O_5$  (Ac) sample is rather featureless, and the absence of hydrogen underpotential deposition features (at potentials < 0.5  $V_{RHE}$ ) confirm the absence of metallic Ir on both catalysts' surfaces.

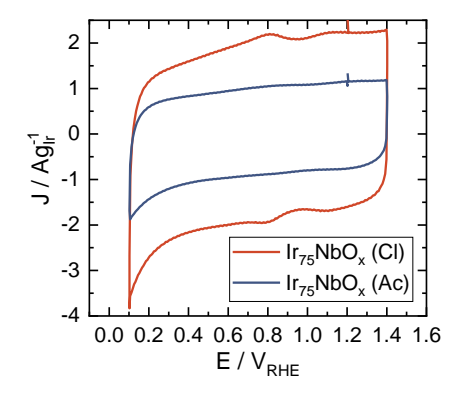
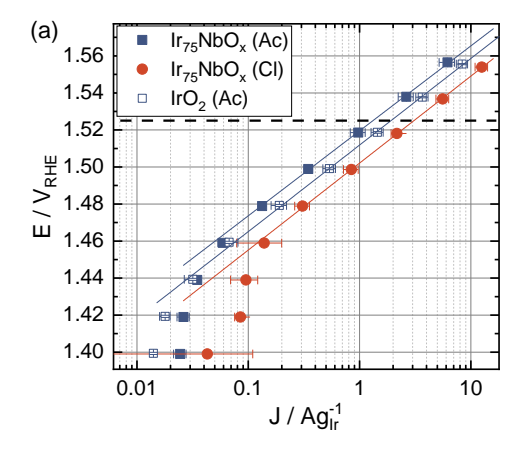


**Figure 1.5.** CVs at 50 mV·s<sup>-1</sup> of  $IrO_2/Nb_2O_5$  (CI) and  $IrO_2/Nb_2O_5$  (Ac).

The catalysts' OER activity was evaluated as the mass normalized current at a potential of  $1.525 \, V_{RHE}$  and, as shown in Figure 1.6a and Table 1.1,  $IrO_2/Nb_2O_5$  (CI) exhibits a higher activity than  $IrO_2/Nb_2O_5$  (Ac). Interestingly, when these currents are normalized by the integrated current in the CVs in Fig. 1.5 (in a 1.0-1.4  $V_{RHE}$  potential window), the OER-activity of these catalysts becomes similar (cf. Fig. 1.6b). Therefore, their surface-specific OER- activity is not sensitive to the type of precursor used in their synthesis, and the differences in mass-normalized activity can be ascribed to the higher surface area of  $IrO_2/Nb_2O_5$  (CI). On the other hand, when comparing the mass specific OER-activity of the  $IrO_2/Nb_2O_5$  (CI) remains the highest.



Interestingly, the Tafel slope in all three materials stays similar, meaning that adding Nb<sub>2</sub>O<sub>5</sub> does not play significant role in OER mechanism.



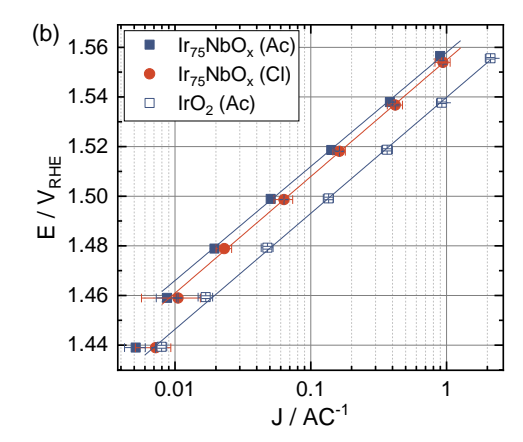


**Figure 1.6.** OER-polarization curves of the three IrOx-based catalysts, with the currents normalized with respect to the catalyst mass (a) or to ther double layer charge (b).

**Table 1.1.** Comparison of the Tafel slopes, OER activity values and stability parameters of the three catalysts.

	Tafel slope / mV·dec <sup>-1</sup>	J at 1.525 V <sub>RHE</sub> / Ag <sub>Ir</sub> -1	E at 10 Ag <sub>ir</sub> -1 / V <sub>RHE</sub>	Current loss at 1.6 V <sub>RHE</sub> after 500 steps / %
IrO <sub>2</sub> /Nb <sub>2</sub> O <sub>5</sub> (Ac)	46	1.3	1.55	62
IrO <sub>2</sub> /Nb <sub>2</sub> O <sub>5</sub> (CI)	47	3.1	1.57	50
IrO <sub>2</sub> (Ac)	47	1.9	1.56	32

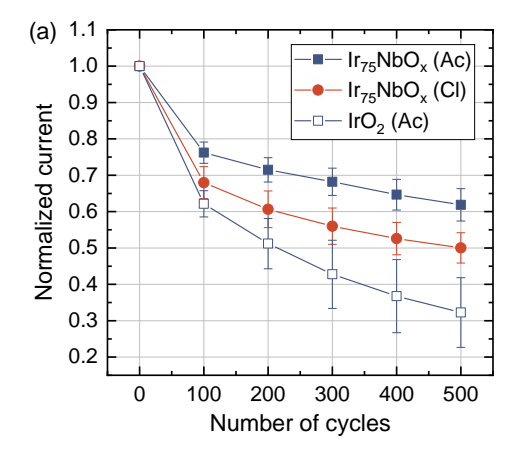
The stability of these catalysts was investigated using an accelerated stress test (AST) that mimics start/stop behavior of an electrolyser, as described in the above experimental section. At the end of the 500 potential steps,  $IrO_2/Nb_2O_5$  (Ac) featured the highest stability (see Figure 1.7a), followed by  $IrO_2/Nb_2O_5$  (CI) and  $IrO_2$  (Ac). Possible changes in the catalysts' surfaces in the course of this AST were assessed by periodically recording CVs, for which the charge every 100 cycles systematically increases with the time / cycle number, as shown in Fig. 1.7b. Interestingly, this behavior is the opposite of what was reported for pure  $IrO_2$  materials synthesized via the Adams fusion method [10]. In order to understand these differences in activity loss among materials, and whether  $Nb_2O_5$  really promotes the durability of  $IrO_2$ , we conducted a systematic study evaluating the possible reasons for this performance loss during the AST.

To this end, one must first consider that the current measured during the AST (i) has to be consistent with Tafel equation:

$$i = j_0 \cdot m \cdot ECSA \cdot e^{\frac{\alpha F}{RT}\eta}$$
 [1]



where,  $j_0$  is the catalyst's exchanged current density in A·cm<sup>-2</sup><sub>cat</sub>, m is the mass of catalyst in g, ECSA stands for the electrochemical surface area in cm<sup>2</sup><sub>cat</sub>·g<sup>-1</sup>,  $\alpha$  is the transfer coefficient, F and R are the Faraday and gas constants, T is the temperature and  $\eta$  refers to the overpotential. Based on this, the current loss along the AST can originate from (i) intrinsic deactivation processes such as a change in the oxidation state or in crystallinity that would lead to a decrease in  $j_0$ , and (ii) a loss of mass and/or ESCA due to morphology change and/or catalyst dissolution. Notably, the later could also arise from artifacts such as mechanical detachment, corrosion of the backing electrode and/or accumulation of micro-/nano- bubbles in the catalyst's pores. In what follows we present investigation of these processes in order to try to break down the AST-induced current losses in these 3 catalysts.



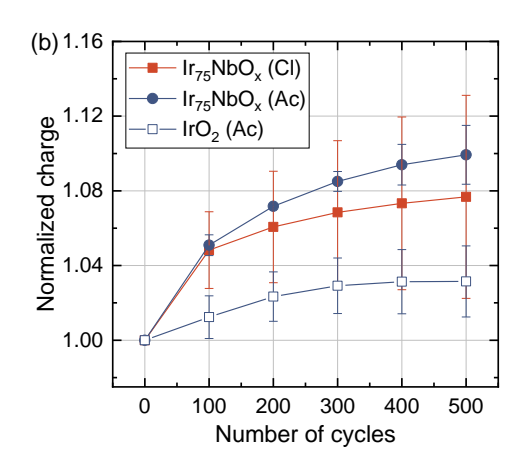


**Figure 1.7.** Evolution of the OER-current normalized with respect to the beginning-of-test value during the AST (a) and of the corresponding double layer charges (also normalized with regards to the beginning-of-test) determined from CVs in the range between 1.0 and 1.4 V<sub>RHE</sub> at 50 mv·s<sup>-1</sup> (b).

The OER-activity of  $IrO_x$ -based catalysts is known to be largely dependent on the oxidation state of Ir active sites on the catalyst's surface [10,28,29]. Therefore, possible changes in the oxidation state of the catalysts during the AST were assessed by *post mortem* XPS. As shown in Figures 1.8a and 1.8b, no changes in oxidation state were observed for either of the catalysts. Moreover, processes that increase the structural disorder of the  $IrO_2$  surface, such as an increase in the Ir-O bond distance with cycling or lattice oxygen evolution [10,29,30] would lead to a surface amorphization that is one of the possible degradation paths. To verify this possibility, we performed *operando* XRD experiment using a flow cell (see above). For this, we investigated the  $IrO_2/Nb_2O_5$  (CI) sample, since XRD is a bulk technique and this material has biggest surface area, this leading to the highest sensitivity to such surface changes. The XRD patterns were recorded while holding at 1  $V_{RHE}$  before starting the AST, after 100 and 500 potential cycles, with acquisition requiring approximately 30min. As illustrated in Figure 1.8c, though, no changes in crystallinity during *operando* XRD study were observed.



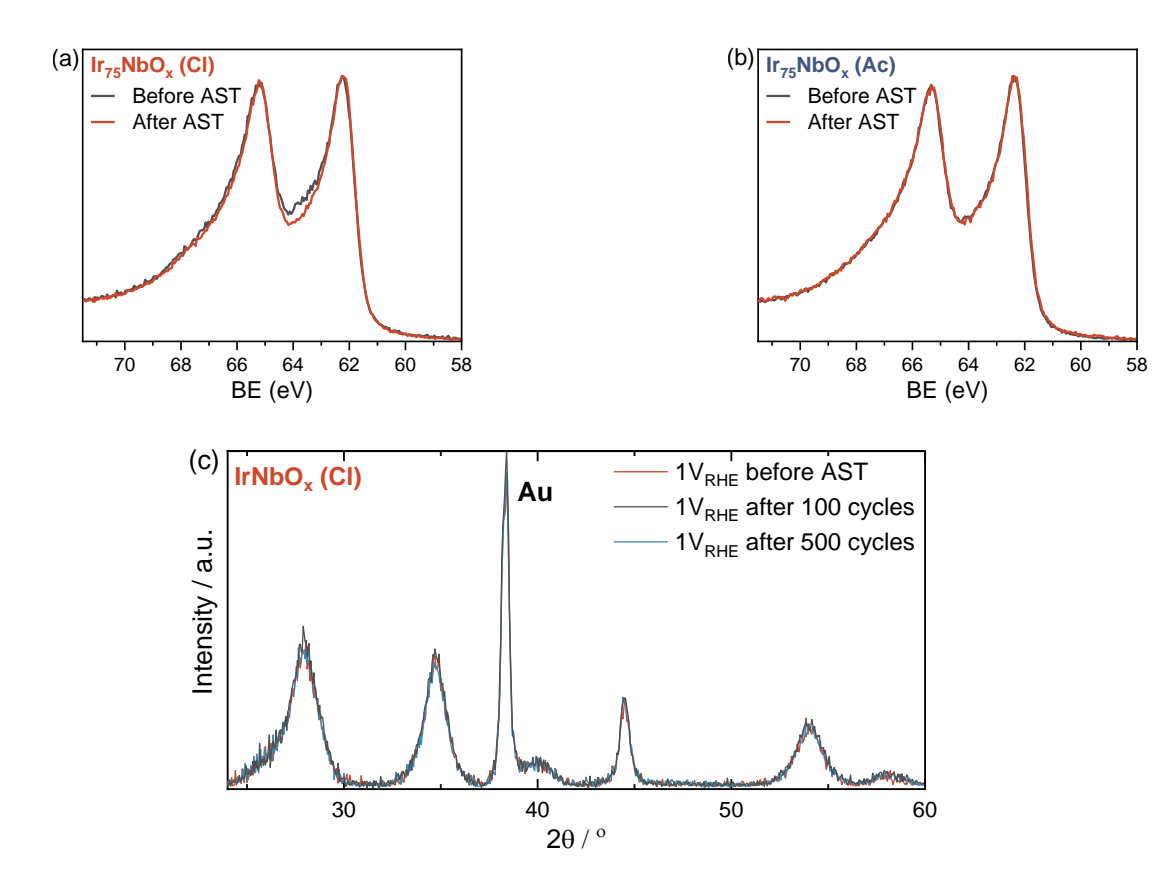


**Figure 1.8.** XP-spectra before and after the AST performed in the flow cell for a)  $IrO_2/Nb_2O_5$  (CI) and b)  $IrO_2/Nb_2O_5$  (Ac). *Operando* XRD of  $IrO_2/Nb_2O_5$  (CI) (c), whereby the diffraction peak assigned to is coming from the sputtered Au layer on the working electrodes.

The occurrence of morphological changes undergone by these materials during the AST were investigated via post mortem TEM. As shown in Figure 1.9, both catalysts are in the form of agglomerated nanocrystals and it is hard to unambiguously conclude that any surface modification took place in the course of the AST. In case of such agglomerates, SEM might be better suited to trace surface changes, and IL measurements are possible without using TEM grid that usually contains a carbon coating that will likely corrode in the curse of the AST potential cycles. Thus, IL-SEM was performed before and after the AST in order to verify surface modifications of the same particles along with the possibility of the particles growing, becoming smaller, moving and/or detaching. IL-SEM micrographs of three material are displayed in Figure 1.10, and show that no morphological differences between specific particles before and after the AST are noticeable. This is in line with previous reports [31] in which the absence of any morphological differences was attributed to low resolution of SEM.



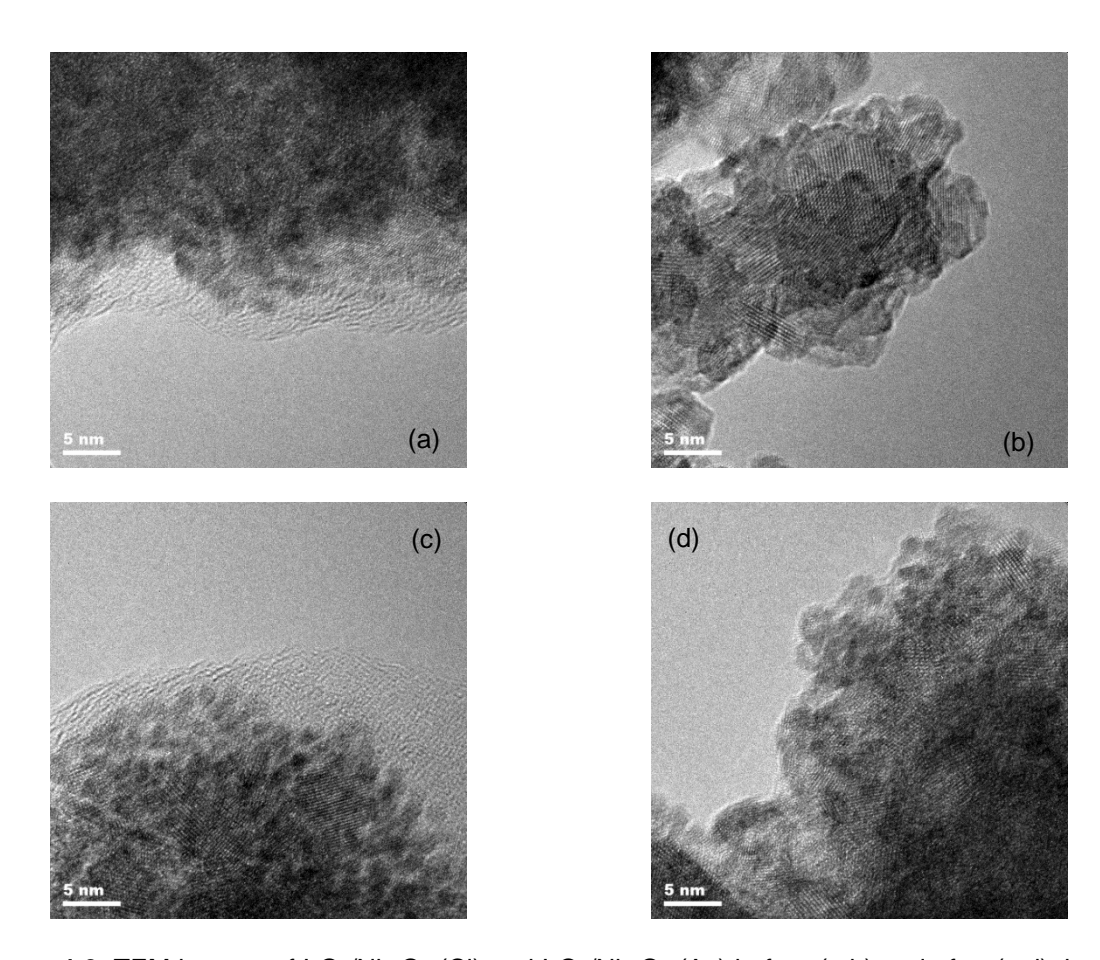


**Figure 1.9.** TEM images of  $IrO_2/Nb_2O_5$  (CI) and  $IrO_2/Nb_2O_5$  (Ac) before (a,b) and after (c,d) the 500 potential cycles of the AST.

On the other hand, IL-SEM images with a lower magnification unveiled that particle migration is visible on all three electrodes. The most distinctive case is that of the inhomogeneous  $IrO_2/Nb_2O_5$  (Ac) sample, in which the  $Nb_2O_5$  particles separated from the  $IrO_2$  phase appear to be prone to detachment upon evolution of  $O_2$  gas on the  $IrO_2$  surfaces below them (see Figure 1.11). Notably, this detachment of  $Nb_2O_5$  particles could lead to more  $IrO_2$  surface being exposed to the electrolyte, which can explain the increase in surface charge discussed above (se Fig. 1.7b).



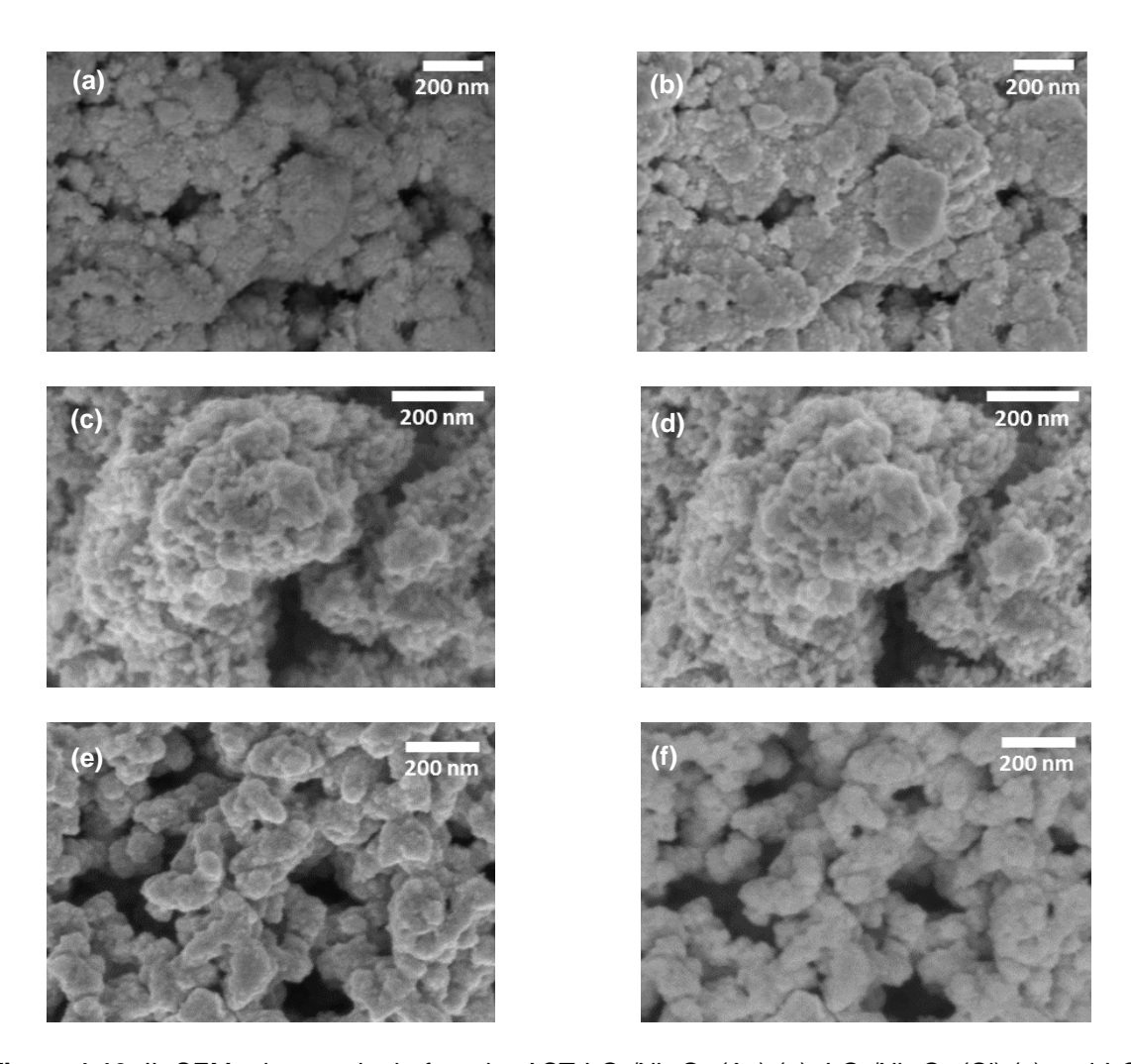


**Figure 1.10.** IL-SEM micrographs before the AST  $IrO_2/Nb_2O_5$  (Ac) (a),  $IrO_2/Nb_2O_5$  (CI) (c) and  $IrO_2$  (Ac) (e), along with the complementing images after 500 potential cycles (b, d and f, respectively).

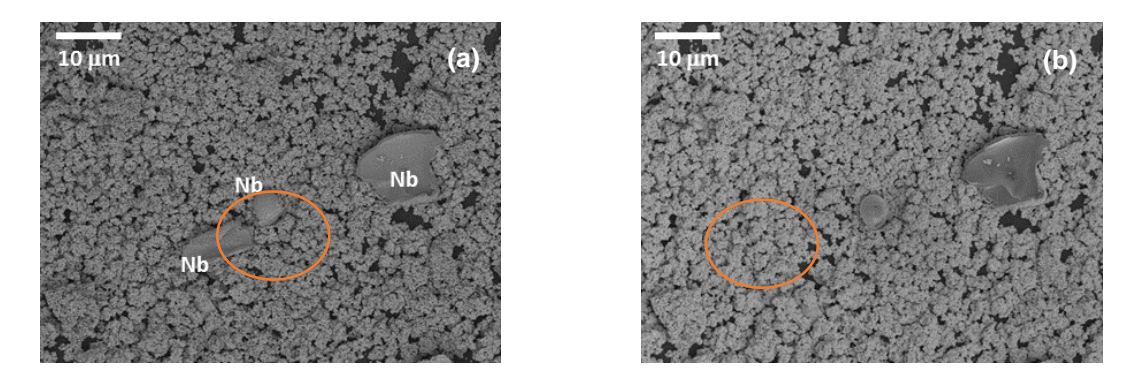


**Figure 1.11.** Low magnification IL-SEM micrographs of  $IrO_2/Nb_2O_5$  (Ac) before (a) and after (b) the AST, showing the detachment of segregated  $Nb_2O_5$  particles



Besides for this detachment of the non-active  $Nb_2O_5$  phase in the case of  $IrO_2/Nb_2O_5$  (Ac), all materials exhibited some extent of delamination of the  $IrO_2$  phase as well. As indicated by the yellow circles in Figure 1.12, some of the catalyst was detached from the electrode, exposing active surface area or just glassy the carbon disk used as the backing electrode. Interestingly, this catalyst detachment is systematically accompanied by the re-deposition of some particles, as indicated by the blue circles in Figure 1.12. Unfortunately, it is hard to quantify the contribution of these processes to the overall current loss observed during the ASTs, but it appears certain that the migration of particles is the dominant process occurring during testing in RDE configuration, as opposed to changes in the catalysts' surface morphology.

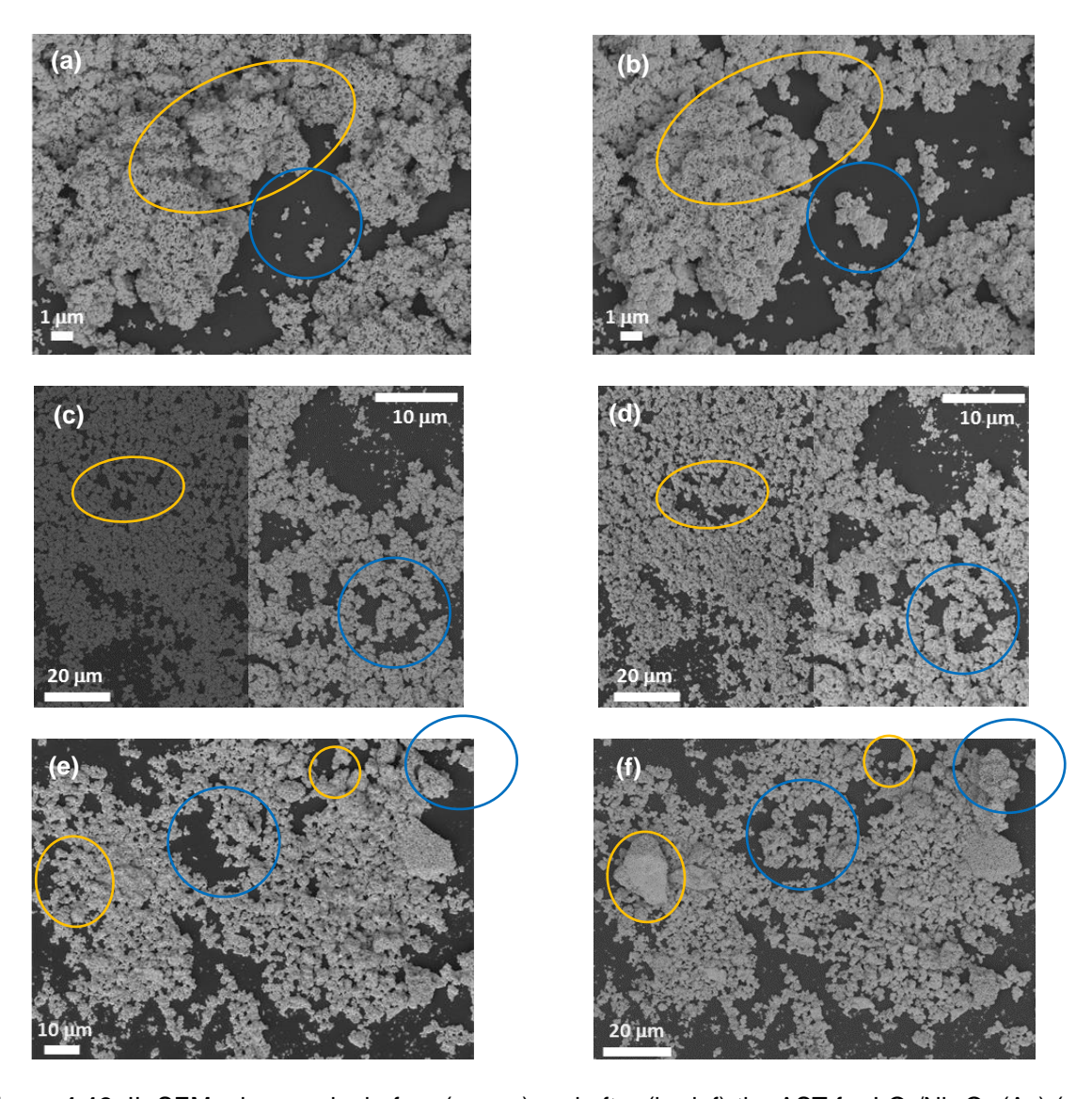
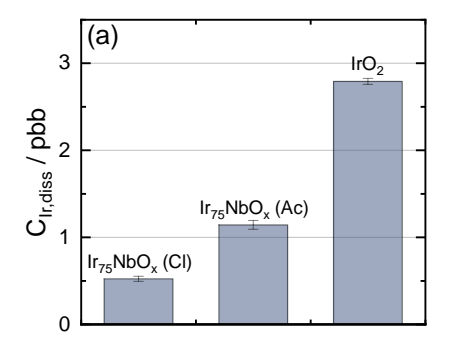


**Figure 1.12.** IL-SEM micrographs before (a, c, e) and after (b, d, f) the AST for  $IrO_2/Nb_2O_5$  (Ac) (a, b),  $IrO_2/Nb_2O_5$  (Cl) (c, d) and  $IrO_2$  (Ac) (e, f).

Currently, the dissolution of Ir is wiedly regarded as a major source of degradation for IrO<sub>2</sub>-based anodes whereby, even if relatively stable, rutile type IrO<sub>2</sub> has been shown to display non-negligible dissolution



[31,32]. In the case of the  $IrO_2/Nb_2O_5$  materials used in this study, both Ir and Nb are detected in the electrolyte after 500 cycles (see Figure 1.13), with pure  $IrO_2$  dissolving the highest amount of Ir, followed by  $IrO_2/Nb_2O_5$  (Ac).  $IrO_2/Nb_2O_5$  (Cl) displays the lowest Ir dissolution extent, which is counterintuitive with regards to the stability results in Figure 1.7. Moreover,  $IrO_2/Nb_2O_5$  (Cl) lost significantly more Nb compared to the material synthesized with the acetate precursor, in agreement with the IL-SEM measurements discussed above, whereby  $IrO_2/Nb_2O_5$  (Ac) experienced significant detachment of of  $Nb_2O_5$  particles that are not detected via ICP-MS (only sensitive to dissolved, ionic species). Considering this,  $IrO_2/Nb_2O_5$  (Ac) contains less  $Nb_2O_5$  participating in the reaction, and at the same time also more  $IrO_2$  exposed to electrolyte.



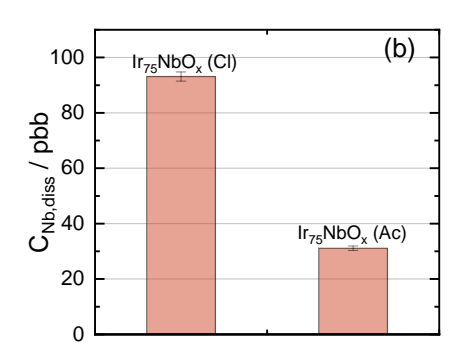


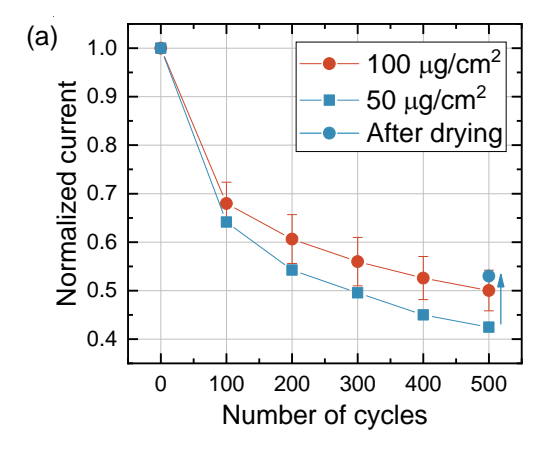
**Figure 1.13.** Concentrations of dissolved Ir (a) and Nb (b) in the electrolyte at the end of the AST for the different catalysts included in this study.

Finally, these ICP-MS results can be used to quantify the percentage of Ir and Nb dissolved from the electrodes. Interestingly this accounts for a 2 % of Nb loss through dissolution in the case of  $IrO_2/Nb_2O_5$  (Ac), and approximately 7 % in the case of  $IrO_2/Nb_2O_5$  (Cl). In contrast, the dissolution of Ir is rather minor for both catalysts, and in the range of 0.004 to 0.02 %. Thus, considering that Ir is the OER-active site, this loss through dissolution cannot explain the significant loss in current observed during the ASTs.

Based on this investigating of the possible deactivation processes that intrinsic to the  $IrO_2/Nb_2O_5$  catalysts, we cannot fully break down the OER-activity losses in Figure 1.7. Therefore, we performed quick tests to investigate possible artifacts compromising the accuracy of these RDE measurements to screen the stability of OER-catalysts [33–35]. To investigate the possible influence of  $O_2$  micro- and nano-bubbles stuck in the pores of the catalyst layer and that would shield its active sites, we performed a new AST on the  $IrO_2/Nb_2O_5$  (CI) catalyst using half of the catalyst loading, as to keep the mass specific current density equal decreasing the geometrical current density, leading to a concomitant decrease of the overall  $O_2$  production rate [33] (and of the chaces of these gas bubbles getting traped in the catalyst layer). Thus, if such oxygen bubbles were to influence the stability of this catalyst, the activity loss in in this measurements with a lower loading should be lower. However, as shown in Fig. 1.14a, the current loss is very similar independently of whether a catalyst loading of 50 or 100  $\mu$ g/cm² is used during the AST, indicating that bubble accumulation does not play major role in this current loss.

Additionally, after 500 cycles, the electrode was dried under vacuum (10<sup>-4</sup> mbar) as to effectively remove any bubbles that may have remained trapped in the catalyst layer. As also shown in Figure 1.14a, though, after restarting the AST protocol on such a vacuum-dried electrode, only 10 % of current recovery was found. This result implies again that bubble accumulation is only occurring to a minor extent, and is not major contribution to the overall activity loss observed during the AST.





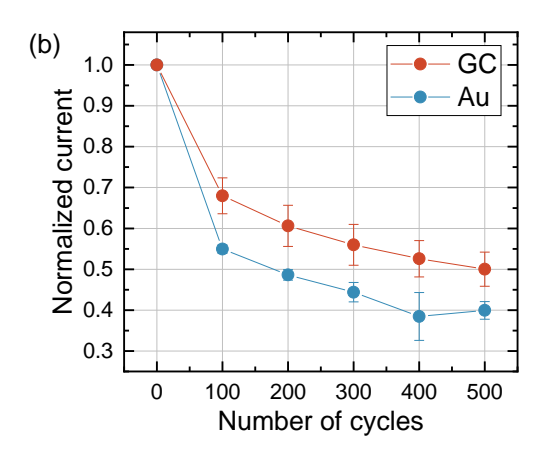


**Figure 1.14.** Comparison of the activity losses along the AST for  $IrO_2/Nb_2O_5$  (CI) 100 vs. 50  $\mu g/cm^2$  loading (a), including the normalized current after the electrode was dried under vacuum. Comparison of the stability using a Au- or a glassy carbon disk as the current collector.

Finally, based on previous results studying the influence of the backing electrode on the OER stability of  $IrO_2$ -based catalysts, we exclude the possibility that the current loss arises from the corrosion of the glassy carbon substrate used in these RDE measurements. As an alternative to this glassy carbon, gold is usually proposed as a suitable backing electrode for investigating OER stability, even though it is known that also Au undergoes a certain extent of dissolution at OER-related potentials and pH 1 [34]. Therefore, the AST was performed on  $IrO_2/Nb_2O_5$  (CI) deposited on a polycrystalline Au disk. As shown in Figure 1.14b, the current loss was even bigger when Au was used as the backing electrode, possibly due to increased catalyst detachment observed by optical microscopy. However, even in this case the extent of this detachment was significantly smaller than 60 % loss of current in the AST, hint that the backing electrode is not major contributor to the activity losses observed in these ASTs.

## 1.4 Conclusions and outlook

In conclusion, we characterized several commercial  $IrO_2$  (/Nb<sub>2</sub>O<sub>5</sub>) catalysts synthesized from different precursors and proved that these precursor have an effect on the catalysts' structure, morphology and OER performance. Specifically, the  $IrO_2/Nb_2O_5$  sample synthesized from a chlorine-based precursor exhibited the highest OER activity compared to  $IrO_2/Nb_2O_5$  (Ac) and the  $IrO_2$  (Ac) used as a standard. On the other hand, the  $IrO_2/Nb_2O_5$  (Ac) catalyst performed the best during the AST, loosing  $\approx$  40 % of its initial OER-current, which nevertheless remain significant for an AST lasting only 3 h since (as compared the service life of an electrolyser, in the range of 5 – 10 years).

In order to understand this differences in the activity loss among catalysts, a systematic study was carried out it in which no deactivation processes relatable to changes in the Ir active sites were found. This can be due to the loss of potential control in case of *post mortem* XPS measurements, or due to the bulk sensitivity intrinsic to (*operando*) XRD. On the other hand, the dissolution of both Ir and Nb affecting all catalysts constitutes a minor contribution to the overall current loss during the ASTs. Interestingly, the migration of particles in the catalyst layer across the electrode surface is shown to be a dominant effect, with particles detaching, redepositing and rearranging themselves, even if no



morphological changes, particle growth and/or roughening of the surface due to the dissolution were observed.

Finally, we evaluated possibility of experimental artifacts causing the activity loss during thses AST measurements. It was demonstrated that bubble accumulation has a small impact on the observed current loss, but due to the low potentials used in this study, its contribution is not major. Specifically, it only accounted for  $\approx 10$ % in case of the most active material,  $IrO_2/Nb_2O_5$  (CI), which means that in the two other materials its impact expected to be even lesser. Complementarily, the influence of glassy carbon corrosion on these instability trends was also excluded based on additional measurements using a polycrystalline Au as substrate for  $IrO_2/Nb_2O_5$  (CI), which indicated no increase in durability when compared to glassy carbon.

As a perspective, quantifying the undetermined contribution of mechanical detachment to the overall OER-activity loss is challenging, but we plan to perform XRF measurements [36] to verify the exact amounts of Ir/Nb on the electrode before and after the AST. Besides for this, glassy carbon corrosion and catalyst dispersion will be investigated in more detail in the future, in an effort to understand and fully break down the activity losses during the AST observed in this study.

#### 1.5 References

- [1] B. Han, M. Risch, S. Belden, S. Lee, D. Bayer, E. Mutoro, Y. Shao-Horn, Screening Oxide Support Materials for OER Catalysts in Acid, J. Electrochem. Soc. 165 (2018) F813–F820.
- [2] Q. Feng, X.Z. Yuan, G. Liu, B. Wei, Z. Zhang, H. Li, H. Wang, A review of proton exchange membrane water electrolysis on degradation mechanisms and mitigation strategies, J. Power Sources. 366 (2017) 33–55.
- [3] E. Oakton, D. Lebedev, M. Povia, D.F. Abbott, E. Fabbri, A. Fedorov, M. Nachtegaal, C. Cope, T.J. Schmidt, IrO2-TiO2: A High-Surface-Area, Active, and Stable Electrocatalyst for the Oxygen Evolution Reaction, ACS Catal. 7 (2017) 2346–2352.
- [4] V.K. Puthiyapura, S. Pasupathi, S. Basu, X. Wu, H. Su, N. Varagunapandiyan, B. Pollet, K. Scott, RuxNb1-xO2 catalyst for the oxygen evolution reaction in proton exchange membrane water electrolysers, Int. J. Hydrogen Energy. 38 (2013) 8605–8616.
- [5] C. Comninellis, G.P. Vercesi, Characterization of DSA-Type electrodes: choice of a coating, J. Appl. Electrochem. 21 (1991) 335–345.
- [6] C. Van Pham, M. Bühler, J. Knöppel, M. Bierling, D. Seeberger, D. Escalera-López, K.J.J. Mayrhofer, S. Cherevko, S. Thiele, IrO2 coated TiO2 core-shell microparticles advance performance of low loading proton exchange membrane water electrolyzers, Appl. Catal. B Environ. 269 (2020) 118762.
- [7] G.C. Da Silva, S.I. Venturini, S. Zhang, M. Löffler, C. Scheu, K.J.J. Mayrhofer, E.A. Ticianelli, S. Cherevko, Oxygen evolution reaction on tin oxides supported iridium catalysts: Do we need dopants?, ChemElectroChem. (2020) 1–47.
- [8] W. Xu, G.M. Haarberg, F. Seland, S. Sunde, A.P. Ratvik, S. Holmin, J. Gustavsson, Å. Afvander, E. Zimmerman, T. Åkre, The durability of the thermally decomposed IrO2 -Ta2O5 coated titanium anode in a sulfate solution, Corros. Sci. 150 (2019) 76–90.
- [9] T. Åkre, E. Zimmerman, F. Seland, J. Gustavsson, G.M. Haarberg, T. Shimamune, A.P. Ratvik, S. Sunde, W. Xu, Calcination Temperature Dependent Catalytic Activity and Stability of IrO2 –



- Ta2O5 Anodes for Oxygen Evolution Reaction in Aqueous Sulfate Electrolytes, J. Electrochem. Soc. 164 (2017) F895–F900.
- [10] M. Povia, D.F. Abbott, J. Herranz, A. Heinritz, D. Lebedev, B.-J. Kim, E. Fabbri, A. Patru, J. Kohlbrecher, R. Schäublin, M. Nachtegaal, C. Copéret, T.J. Schmidt, Operando X-ray characterization of high surface area iridium oxides to decouple their activity losses for the oxygen evolution reaction, Energy Environ. Sci. 12 (2019) 3038–3052.
- [11] A.J. Terezo, E.C. Pereira, Fractional factorial design applied to investigate properties of Ti/IrO2-Nb2O5electrodes, Electrochim. Acta. 45 (2000) 4351–4358.
- [12] A. Zlotorowicz, F. Seland, S. Sunde, Composite Thin Film Iridium- Niobium Oxide Electrocatalysts for the Oxygen Evolution Electrode, J. Eur. Ceram. Soc. 50 (2013) 71–84.
- [13] T. Binninger, E. Fabbri, A. Patru, M. Garganourakis, J. Han, D.F. Abbott, O. Sereda, R. Kötz, A. Menzel, M. Nachtegaal, T.J. Schmidt, Electrochemical Flow-Cell Setup for In Situ X-ray Investigations, J. Electrochem. Soc. 163 (2016) H913–H920.
- [14] No Title, (n.d.) http://www.casaxps.com/.
- [15] D.A. Shirley, High-resolution x-ray photoemission spectrum of the valence bands of gold, Phys. Rev. B. 5 (1972) 4709–4714.
- [16] J.H. Scofield, Hartree-Slater subshell photoionization cross-sections at 1254 and 1487 eV, J. Electron Spectros. Relat. Phenomena. 8 (1976) 129–137.
- [17] V. Pfeifer, T.E. Jones, J.V. Vélez, C. Massué, R. Arrigo, D. Teschner, F. Girgsdies, M. Scherzer, M.T. Greiner, J. Allan, M. Hashagen, G. Weinberg, S. Piccinin, M. Hävecker, A. Knopgericke, R. Schlögl, The electronic structure of iridium and its oxides, 48 (2016) 261–273.
- [18] G.K. Wertheim, H.J. Guggenheim, Conduction-electron screening in metallic oxides: IrO2, Phys. Rev. B. 22 (1980) 4680–4683.
- [19] S.J. Freakley, J. Ruiz-Esquius, D.J. Morgan, The X-ray photoelectron spectra of Ir, IrO2 and IrCl3 revisited, Surf. Interface Anal. 49 (2017) 794–799.
- [20] A.H. Clark, J. Imbao, R. Frahm, M. Nachtegaal, ProQEXAFS: A highly optimized parallelized rapid processing software for QEXAFS data, J. Synchrotron Radiat. 27 (2020) 551–557.
- [21] M. Newville, IFEFFIT: Interactive XAFS analysis and FEFF fitting, J. Synchrotron Radiat. 8 (2001) 322–324.
- [22] R.J. Cava, B. Batlogg, J.J. Krajewski, H.F. Poulsen, P. Gammel, W.F. Peck, L.W. Rupp, Electrical and magnetic properties of Nb2O5-δ crystallographic shear structures, Phys. Rev. B. 44 (1991) 6973–6981.
- [23] M.A. Aegerter, Sol-gel niobium pentoxide: A promising material for electrochromic coatings, batteries, nanocrystalline solar cells and catalysis, Sol. Energy Mater. Sol. Cells. 68 (2001) 401–422.
- [24] G. Greczynski, L. Hultman, X-ray photoelectron spectroscopy: Towards reliable binding energy referencing, Prog. Mater. Sci. 107 (2020) 100591.
- [25] J.H. Sinfelt, G.D. Meitzner, X-ray Absorption Edge Studies of the Electronic Structure of Metal Catalysts, Acc. Chem. Res. 26 (1993) 1–6.
- [26] T. Tanaka, T. Yoshida, H. Yoshida, H. Aritani, T. Funabiki, S. Yoshida, J.M. Jehng, I.E. Wachs, XAFS study of niobium oxide on alumina, Catal. Today. 28 (1996) 71–78.
- [27] A.R. Hillman, M.A. Skopek, S.J. Gurman, X-ray spectroscopy of electrochemically deposited iridium oxide films: Detection of multiple sites through structural disorder, Phys. Chem. Chem. Phys. 13 (2011) 5252–5263.



- [28] V.A. Saveleva, L. Wang, D. Teschner, T. Jones, A.S. Gago, K.A. Friedrich, S. Zafeiratos, R. Schlo, E.R. Savinova, Operando Evidence for a Universal Oxygen Evolution Mechanism on Thermal and Electrochemical Iridium Oxides, (2018).
- [29] D.F. Abbott, D. Lebedev, K. Waltar, M. Povia, M. Nachtegaal, E. Fabbri, C. Copéret, T.J. Schmidt, Iridium oxide for the oxygen evolution reaction: Correlation between particle size, morphology, and the surface hydroxo layer from operando XAS, Chem. Mater. 28 (2016) 6591–6604.
- [30] K. Schweinar, B. Gault, I. Mouton, O. Kasian, Lattice Oxygen Exchange in Rutile IrO2during the Oxygen Evolution Reaction, J. Phys. Chem. Lett. 11 (2020) 5008–5014.
- [31] P. Jovanovič, N. Hodnik, F. Ruiz-Zepeda, I. Arčon, B. Jozinović, M. Zorko, M. Bele, M. Šala, V.S. Šelih, S. Hočevar, M. Gaberšček, Electrochemical Dissolution of Iridium and Iridium Oxide Particles in Acidic Media: Transmission Electron Microscopy, Electrochemical Flow Cell Coupled to Inductively Coupled Plasma Mass Spectrometry, and X-ray Absorption Spectroscopy Study, J. Am. Chem. Soc. 139 (2017) 12837–12846.
- [32] O. Kasian, J. Grote, S. Geiger, S. Cherevko, K.J.J. Mayrhofer, The Common Intermediates of Oxygen Evolution and Dissolution Reactions during Water Electrolysis on Iridium, (2018) 2488–2491.
- [33] H.A. El-Sayed, A. Weiß, L.F. Olbrich, G.P. Putro, H.A. Gasteiger, OER Catalyst Stability Investigation Using RDE Technique: A Stability Measure or an Artifact?, J. OfThe Electrochem. Soc. 166 (2019) 458–464.
- [34] S. Geiger, O. Kasian, A.M. Mingers, S.S. Nicley, K. Haenen, K.J.J. Mayrhofer, S. Cherevko, Catalyst Stability Benchmarking for the Oxygen Evolution Reaction: The Importance of Backing Electrode Material and Dissolution in Accelerated Aging Studies, ChemSusChem. 10 (2017) 4140–4143.
- [35] A. Hartig-Weiss, M.F. Tovini, H.A. Gasteiger, H.A. El-Sayed, OER Catalyst Durability Tests Using the Rotating Disk Electrode Technique: The Reason Why This Leads to Erroneous Conclusions, ACS Appl. Energy Mater. (2020) acsaem.0c01944.
- [36] M. Chourashiya, R. Sharma, S.M. Andersen, Accurate Determination of Catalyst Loading on Glassy Carbon Disk and Its Impact on Thin Film Rotating Disk Electrode for Oxygen Reduction Reaction, Anal. Chem. 90 (2018) 14181–14187.



## Part 2.- Commercial iridium oxide catalysts for H<sub>2</sub>-starvation in polymer electrolyte fuel cell anodes

## 2.1 Introduction

During normal operation of a polymer electrolyte fuel cell (PEFC), the anode is supplied with hydrogen and the cathode with air. During operation, it can happen that a drop of water forms on the anode, blocking a flow channel and therefore cutting the hydrogen supply [1-4]. Without the reactant, the anode cannot provide the current at normal operation potentials and the other stack cells connected in series polarize this hydrogen starved anode until another reaction supplies the current required by the stack. For state of the art anode catalysts, this reaction is the corrosion of the carbon support of the Pt/C catalysts customarily used for H<sub>2</sub>-oxidation. For typical state-of-the-art anodes containing 0.1 mg<sub>carbon</sub>/cm<sup>2</sup>, this carbon inventory would be consumed within seconds in case of a hydrogen starvation event at an operation current of 0.5 A/cm<sup>2</sup>, leading to a complete failure of the starved cell. This drastic degradation is one of the main lifetime issues that PEFCs face today. According to industry sources, engineering solutions do not seem to be feasible and membrane electrode assembly (MEA-) based solutions are urgently required [1]. Adding an OER catalyst to the anode, which favors OER over the carbon oxidation reaction (COR) and therefore enhances the lifetime of a hydrogen-starved cell, is one of the most promising approaches found in patents and literature.

Thus, the second part of the project explores the use of the IrO<sub>2</sub>/NbO<sub>x</sub> catalysts featured in Part 1 as additives for PEFC anodes to mitigate their degradation during hydrogen starvation and investigate which properties of these co-catalysts as well of the catalyst layer influence the effectiveness of this approach. The behavior of the co-catalysts under normal operation conditions was first investigated in an RDE configuration in which no major differences were observed (see 2019 report). On this basis, general considerations about the feasibility of the co-catalyst approach led us to the conclusion that the amount of water present in the anode is probably a major limiting factor that has not been considered in the published literature and could be a bottleneck for the application. This effect is now experimentally proved in this report, in which we also describe for the first time an unreported stability issue for ultra-low-loaded anode catalysts. Note that the experimental infrastructure to elucidate the importance of water, the suitability of the starvation test protocols currently employed in the literature and the impact of the new stability mechanism described below are currently being built up.

## 2.2 Experimental section

Fuel cell preparation.— Catalyst-coated membranes (CCMs) were prepared via spray coating at 50°C using an appropriate ink formula, as reported in [5]. The catalyst loading was controlled by the amount of sprayed layers, and monitored through the weight change of a reference sheet. MEAs were prepared by hotpressing two gas diffusion layers (GDL) (Freudenberg H24C5) at 140°C and 4 bar. The compression of the GDLs in the assembled cells was controlled via metal spacers and adjusted to 25%.

Starvation tests. – Starvation tests were carried out at 80°C, 1.5 bar absolute pressure at 100% relative humidity (RH). The current was set to 0.2 or 0.6 A/cm² and the nitrogen or hydrogen flow rate was adjusted to yield the desired stoichiometry. To proof the existence of the trapped state described below, the flow was switched between humidified nitrogen and hydrogen



## 2.3 Results and discussion

#### 2.3.1 Water management

The OER taking place at a given co-catalyst surface (through  $H_2O$  -->  $O_2$  +  $2H^+$  +  $2e^-$ ) implies the consumption of water in case of a starvation event. The availability of water for the catalyst is therefore a necessity and will have a decisive impact on the feasibility of this approach. Water also hydrates the ionomer and determines its proton conductivity, and its availability depends on the cell's operative relative humidity. When the OER co-catalyst consumes water, the ionomer will replace consumed water by taking up water from the gas phase, which will lead to a change in water partial pressure (and therefore relative humidity) close to the co-catalyst surface. All of these parameters are highly important for the performance of the co-catalyst, but their close correlation also highlights the complexity of the performance-determining processes of an OER co-catalyst system. Thus, the first goal of the project was to define meaningful test conditions and to experimentally prove that the existing test protocols do not accurately reflect the impact of water on the starvation process and need to be revised.

Typical test protocols mimic a starvation event by supplying humidified nitrogen to the anode while drawing a certain current (usually 200 mA/cm²) which under starvation conditions cannot be produced via hydrogen oxidation. The problem of this approach is twofold. First, previous publications did not systematically monitor and normalize the nitrogen flow rate, which would have been necessary to control the water supply. As demonstrated in Fig. 2.1, a change in the nitrogen flow rate has a significance impact of the reversal tolerance time. The second problem is that mimicking the starvation by substituting  $H_2$  with  $N_2$  implies a constant supply of water, while in a real starvation event forst the remaining hydrogen and then the water will be consumed. This will lead to drastically different flow conditions within the channels and will alter mass transport effects.

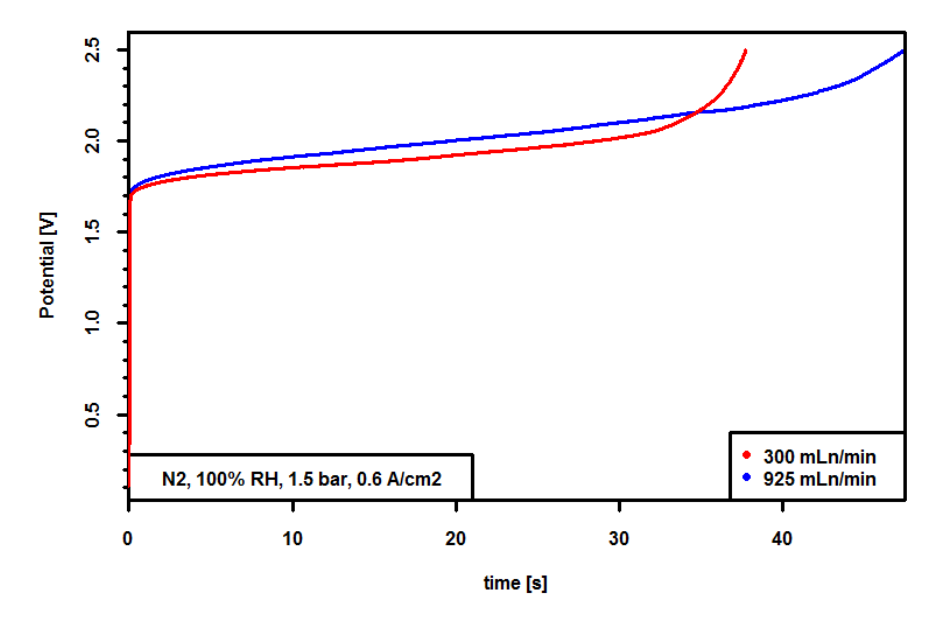


**Figure 2.1.** Effect of the nitrogen flow on the reversal tolerance of 0.1  $mg_{Pr}/cm^2$  anodes with 0.010  $mg_{Ir}/cm^2$  Ir-oxide co-catalysts, tested by monitoring the current response flowing fully humidified  $N_2$  vs  $H_2$  at anode vs. cathode, respectively, and applying a constant current of 0.6 A/cm<sup>2</sup>.



Based on these considerations, we postulate that test conditions for  $H_2$ -starvation events should be kept as close as possible to the real conditions. To be explicit, one should use humidified hydrogen in a substoichiometric supply to assess the reversal tolerance. We do not exclude that there are model conditions that allow entangling some of the connected properties mentioned in the previous paragraph. Such model conditions are highly desirable but the complexity of the system makes their design challenging.

Another level of complexity is added by the variety conditions of a starvation event. According to literature, gross hydrogen starvation could happen during freeze start, due to blocked hydrogen channels or sudden load demand. This spans a broad variety of conditions like temperature, relative humidity, sub-stoichiometry and reversal time/current. For some of these conditions the OER co-catalyst approach may be not suited, for example when no gas whatsoever (and therefore no OER-reactant, i.e., water) is supplied at all. The second goal of the project is therefor to elucidate the boundaries of the co-catalyst approach by creating a map like the one shown in Fig. 2.2 and marking the condition areas according to the feasibility of the co-catalyst approach.

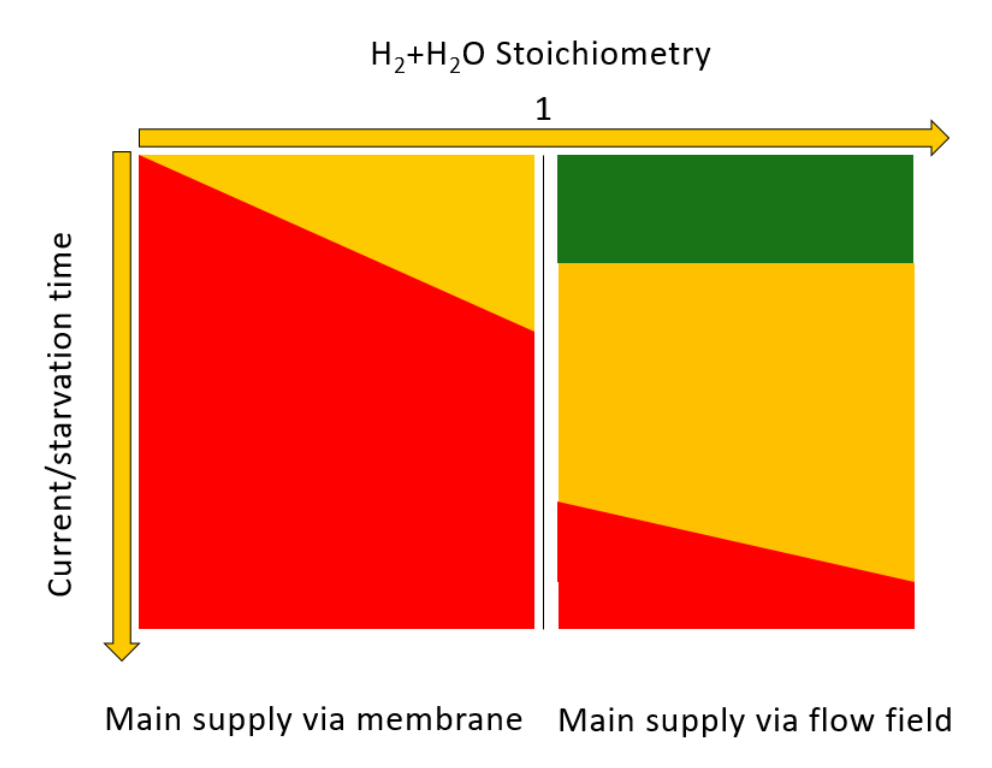


**Figure 2.2.** Estimated feasibility regime for OER co-catalyst systems for cell reversal. Red regimes signal no expected improvements in tolerance upon addition of an OER co-catalyst, yellow ones moderate improvements, and green ones mark regions where the co-catalysts system could possible significantly reduce the corrosion of an anode during the starvation event.

So far, the areas indicated in the figure are only estimated and further experiments will specify the boundaries. We anticipate that carbon corrosion will never be completely suppressed and prolonged reversal time/current will always lead to cell damage. If not enough water is supplied to the OER co-catalyst system the remaining current still has to be supplied via carbon corrosion and will therefore damage the cell. The more severely the hydrogen supply is reduced, the less will the co-catalyst system be able to mitigate the reversal and eventually fail completely below a critical value. Therefore, one of the major challenges of the project is to clarify the boundaries indicated in Fig. 2.2.



#### 2.3.2 Reversal trapped state

During cell reversal the potential of the anode increases, not only triggering carbon corrosion and water oxidation, but also the oxidation of the surface of the platinum catalyst. Notably, the hydrogen oxidation reaction (HOR-) activity of such platinum oxide (PtO) is significantly lower than that of the platinum metal (Pt<sup>0</sup>) on which the HOR customarily takes place. Most importantly, this platinum oxide is reduced only at potentials < 0.8 V<sub>RHE</sub>, whereas carbon corrosion and water oxidation only onset at ≈ 1.5 V<sub>RHE</sub>. The only reaction that could occur below 1.5 V<sub>RHE</sub> is the HOR, but with the reduced activity of platinum oxide it may be possible that the system will not be able to provide the necessary stack current even if the hydrogen supply returns to normal. We were able to prove the existence of this so-called trapped state, illustrated in Fig. 2.3, by switching the anode feed from humidified hydrogen to nitrogen, then back to H<sub>2</sub>, while applying a current of 0.6 A/cm<sup>2</sup>. . Since a few minutes of cell reversal will always result in significant cell damage, such a trapped state is a major corrosion problem for fuel cell anodes. Our experiments so far indicate that this trapped state will occur for ultra-low-loadings (< 50 µgp/cm²), that industry does not reach so far due to the lacking contamination tolerance of current anode catalysts, but that constitutes a major goal of the fuel cell sector. To the best of our knowledge, this trapped state had never been previously described, and represents a major limitation for ultra-low loaded platinum anodes that must be addressed if one intends to further reduce the anode loading without significantly reducing its lifetime. Further experiments will investigate the HOR activity of PtO as well as the oxidation kinetics of platinum to further elucidate the starvation and anode loadings that could lead to such a trapped state.

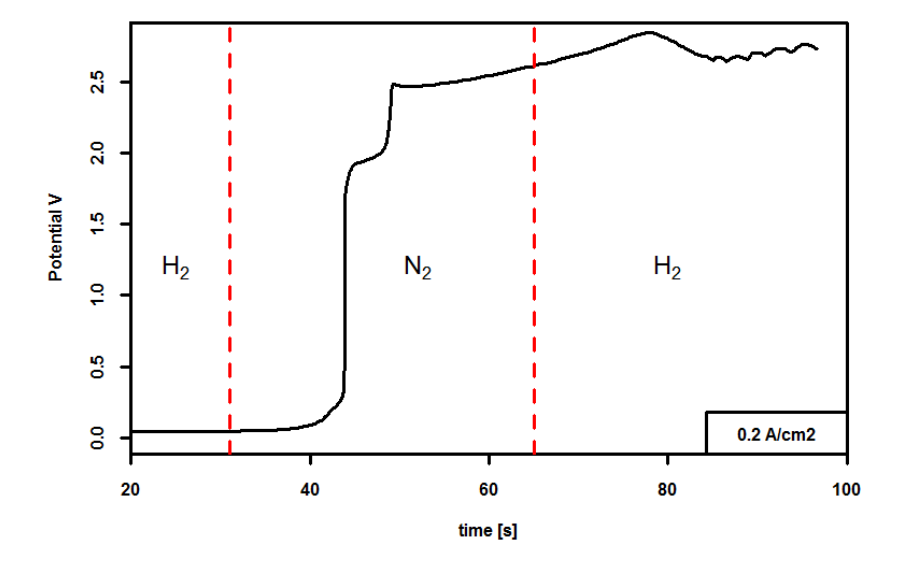


**Figure 2.3.** Experimental proof of the trapped state. When the gas is switched from hydrogen to nitrogen the potential increases until another reaction, mainly carbon corrosion, supplies the current. When the gas is then switched back to hydrogen, the potential does not drop back close to 0 V, which would be normal operation, since the oxidized platinum state concomitant to the N<sub>2</sub>-fed step is not active enough for hydrogen oxidation, and there is no driving force for its reduction back to Pt<sup>0</sup>.

## 2.4 Conclusions and outlook

In conclusion, we were able to demonstrate the so far overlooked complexity of the OER co-catalyst anode system and the unsuitability of commonly used test protocols. We could experimentally prove a so far unknown durability challenge for ultra-low-loaded anodes, that we refer to as starvation trapped state. The latter constitutes a further limitation (on top of contamination tolerance) that must be



addressed in the future to achieve lower platinum anode ladings. The remaining goals of the project are to clarify the complex role of water in an OER co-catalyst anode under reversal conditions, to clarify the boundary conditions under which an OER co-catalyst system can effectively mitigate cell reversal damage, and to elucidate the reversal conditions and anode loadings that can lead to such a reversal trapped state.

## 2.5 References

- [1] P. Mandal, B. K. Hong, J. G. Oh, S. Litster, Understanding the Voltage Reversal Behavior of Automotive Fuel Cells, J. Power Sources 397 (2018) 397–404.
- [2] L. Hu, B. K. Hong, J. G. Oh, S. Litster, Investigation of Hydrogen Stravation of Polymer
   Electrolyte Fuel Cells in Freezing Condition Using Reference Electrode, ECS Transactions 80 (2017)
- [3] T. R. Ralph, S. Hudson, D. P. Wilkinson, Electrocatalyst Stability in PEMFCs and the Role of Fuel Starvation and Cell Reversal Tolerant Anodes, ECS Transactions 1 (2006) 67-84.
- [4] J. Zhang, J. E. Owejan, Ionic Layer with Oxygen Evolution Reaction Catalyst for Electrode Protection, US patent 2010/0178582 A1
- [5] S. Kabir, D. J. Myers, N. Kariuki, J. Park, G. Wang, A. Baker, N. Macauley, R. Mukundan, K. L. More, K. C. Neyerlin, Elucidating the Dynamic Nature of Fuel Cell Electrodes as a Function of Conditioning: An ex Situ Material Characterization and in Situ Electrochemical Diagnostic Study, ACS Appl. Mater. Interf., 11 (2019), 45016–45030



## Part 3.- Combining SAXS and XAS to study *in-house*, high surface area iridium oxides

### 3.1 Introduction

While the commercial Ir-oxides discussed in the above sections consist of highly agglomerated particles displaying a relatively low surface area (SA)  $\leq 20$  -  $30 \text{ m}^2 \cdot \text{g}^{-1}$ , oxides with higher dispersion (and concomitantly greater OER-activities) can be produced using labs-cale synthetic methods. As a result, such high surface area materials san significantly decrease the contribution of the OER process to the device's overall efficiency losses, positively impacting electrolyzers' performance and its commercialization potential.

A proven approach to produce such high-SA oxides is the so-called modified Adams' fusion method presented in a recent study by our group [1], that can yield materials with > 100 m²·g⁻¹. However, such high-SA catalysts often suffer from a poor stability that can be improved by submitting them to a post-synthesis heat-treatment, if at the expense of a decrease in surface area and catalytic performance. To shed light on these differences among as-synthesized and heat-treated materials, in this study we combined small angle X-ray scattering (SAXS) and X-ray absorption spectroscopy (XAS) to assess the *operando* changes in morphology and composition undergone by both catalysts in the course of an accelerated stress test (AST) that mimics PEM-electrolyzer start-up/shut-down. The results derived from the use of these complementing, synchrotron-assisted techniques provided unprecedented insight on the reactivity and stability of these oxides.

## 3.2 Experimental section

Catalyst synthesis. – A high-SA iridium oxide was synthetized by a modified, chlorine-free Adams fusion method [1]. To this end, 300 mg of Ir(III) acetylacetonate (Ir(acac)<sub>3</sub>, 98% Ir, Strem Chemicals) and 10 g of NaNO<sub>3</sub> (>99.5%, Sigma Aldrich) were homogenized by grinding in an agate mortar. The powder mixture was transferred to a porcelain crucible and successively into a muffle furnace where it was heat-treated for 30 min at 350 °C. A fraction of the resulting, as-synthesized sample (referred to as IrO<sub>2</sub>-AS in the following) was additionally heat-treated in a tubular furnace at 400° C in atmospheric air for 1 h to produce the sample IrO<sub>2</sub>-HT.

Electrochemical testing.– Following the procedures detailed in Ref. 4, both catalysts were processed into inks for rotating disc and *operando* flow cell electrodes with  $IrO_x$ -loadings of 0.1 vs. ≈ 4.0 mg·cm<sup>-2</sup>, respectively. All electrochemical measurements were performed at room temperature, using 0.1 M HCIO<sub>4</sub> prepared from 60 % HCIO<sub>4</sub> (Kanto Chemical Co., Inc.) in ultrapure water (18.2 MΩ·cm, ELGA Purelab® Ultra) as the electrolyte.

For rotating disc electrode (RDE) measurements, a 5 mm diameter glassy carbon electrode coated with catalyst was mounted on a vertical shaft (PINE Research Instrument, Inc.) and connected to a BioLogic VMP-300 potentiostat. The shaft was inserted in a standard three-electrode glass cell with a gold mesh as counter electrode and an Hg/HgSO<sub>4</sub> reference electrode pre-calibrated against the reversible hydrogen electrode (RHE) scale. Polarization curves were recorded by increasing the potential stepwise



from 1.2 to 1.6 V vs. RHE, holding at each potential for 1 min while rotating the electrode at 1,600 rpm. The AST consisted of a 500 square potential steps in which the potential is increased from 1.0 to 1.6 V vs. RHE, and held at each of these values for 10 seconds.

Operando SAXS and XAS measurements were performed with the flow cell developed by Binninger *et al.* [2], using a syringe pump (Legato 110 by Kd Scientific) at a withdrawal flow rate of 50 μL·min<sup>-1</sup> to flow electrolyte through the cell. The flow cell was also equipped with a low-leak, 2 mm diameter Ag/AgCl reference electrode (Harvard Apparatus, pre-calibrated vs. RHE), and a counter electrode consisting of a Nafion-immobilized, high-surface area carbon black. The *operando* AST applied during SAXS and XAS measurements was identical to the RDE-one, if including pauses during which SAXS and XAS were acquired while holding the potential at 1.0 V vs. RHE.

Combined SAXS and XAS measurements and data processing.- Combined SAXS and XAS measurements were performed at the SuperXAS beamline of the Swiss Light Source (SLS - Villigen PSI, Switzerland). The novel setup built to this end appears schematized in Figure 3.1, and consists of three ion chambers and a reference sample for the XAS measurement, as well as a flight tube, a beam stopper and a Pilatus 100K 2D-detector for SAXS-acquisition. Following the X-ray path from left to right, a first ion chamber measures the intensity of the incoming beam and is followed by the operando flow cell. The flight tube and remaining ion chambers are placed on a mechanical platform that moves perpendicular to the beam direction, allowing to place these elements along the beam path as to perform XAS or SAXS measurements. The apparatus and the detector calibration procedure are extensively described in the Ref. 3. Structural characterization was perform within an energy range corresponding to the Ir-L<sub>3</sub> edge (at 11.215 keV); specifically, SAXS patterns were acquired 11.1600 and 11.2100 keV (with an exposition time of 1 s), whereas for XAS measurements the monochromator scanned the photon energy range from 300 eV below to 630 eV above the Ir-L<sub>3</sub> edge. The procedures used to treat the resulting SAXS and XAS data can be found in Ref. 3, whereby the subtractive approach of the energy-dependent SAXS curves followed to isolate the scattering contribution of the IrOx-catalysts is explained in detail.

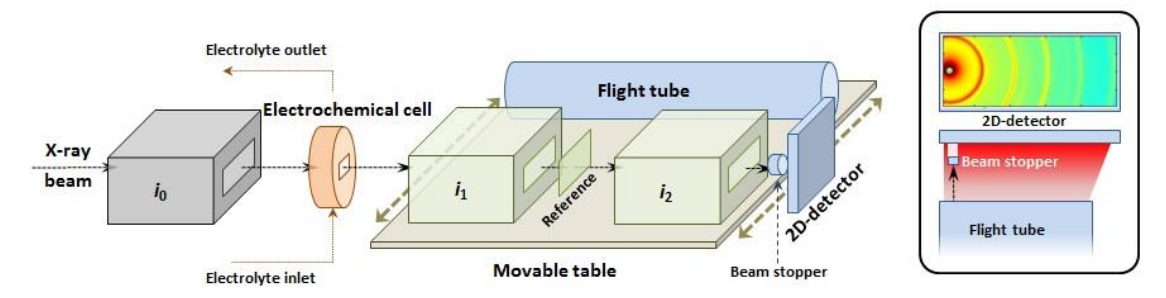


**Figure 3.1.** Schematic representation of the combined SAXS and XAS setup, whereby the gas ionization detectors  $i_1$  and  $i_2$  and an energy-calibration standard (cf. "Reference") are mounted parallel to the flight tube, and all four elements are set on a motorized stage that can be moved perpendicular to the beam direction. For XAS experiments, the incident X-ray intensity is first determined in a gas ionization detector ( $i_0$ ), followed by the analyte mounted in an electrochemical flow cell and gas ionization detectors  $i_1$  and  $i_2$ , which quantify the intensity of the attenuated beam prior to and after absorption through the reference, respectively. For SAXS, the scattered signal travels through a 580 mm long flight tube (evacuated to  $\approx 10^{-3}$  mbar) and is projected on a planar, 2Ddetector protected by a beam-stopper.



## 3.3 Results and discussion

#### 3.3.1 Materials' characterization and electrochemical behaviour

The as-synthesized and heat-treated oxides were first characterized using transmission electron microscopy (TEM), which unveiled that the  $IrO_2$ -AS sample consisted of relatively well dispersed,  $\approx 2$  nm nanoparticles, while its heat-treated derivative ( $IrO_2$ -HT) displays a much larger extent of agglomeration among the oxide particles.

Next, the OER-activity and durability of the two catalysts were determined through electrochemical tests in RDE-configuration. As depicted in Figure 3.2a, the OER-current at 1.5 V vs. RHE is  $\approx$  4-fold larger for the as-synthesized vs. the heat-treated catalyst, but this difference that cannot be solely explained on the basis of the  $\approx$  50 % larger surface are displayed by the as-synthesized catalyst, and must therefore be partially related to intrinsic differences among these materials' surface reactivities (*vide infra*).

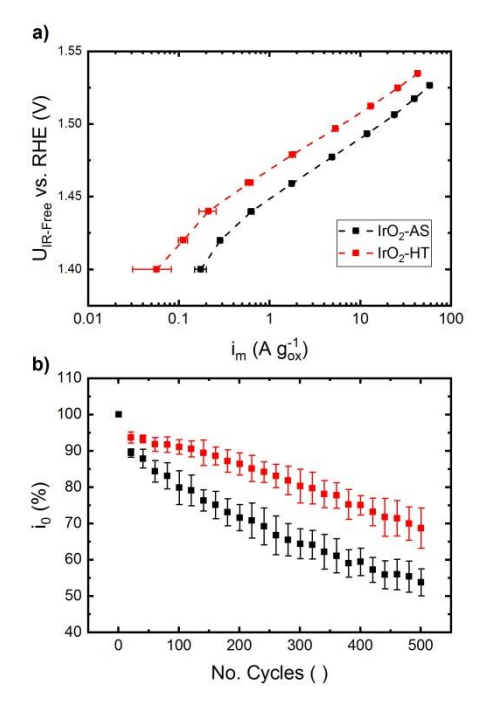


**Figure 3.2.** Beginning-of-life Tafel plots displaying the mass-normalized OER-activity of the two iridium oxides, as derived from RDE measurements in air-saturated 0.1 M HClO<sub>4</sub> (a). Corresponding decay of the OER-current at 1.6 V vs. RHE (normalized with respect to the beginning-of-life value) in the course of the AST (see experimental section for details).

As for the oxides' stability, Figure 3.2b displays the progressive decay of catalytic performance undergone by both catalysts in the course of the electrochemical AST. Notably, the OER-activity of IrO<sub>2</sub>-AS decreased to  $\approx 55$  % of its initial value after 500 potential cycles, whereas IrO<sub>2</sub>-HT only lost  $\approx 30$  % of its activity in the same cycling span. Since these activity/stability trends may be related to *operando* changes in the catalysts' composition and/or morphology, we decided to study these variables using the combined SAXS and XAS setup available at the SLS's SuperXAS beamline.



#### 3.3.2 Operando compositional changes assessed by XAS

As we have discussed in section 1, the Ir-L<sub>3</sub> XANES probes electronic transitions from occupied 2p orbitals to partially filled 5d ones and, as a result, the so-called white line intensity (i.e., the magnitude of the XANES' maximum) is directly proportional to iridium's oxidation state [1]. Considering this, the *operando* XANES for the two iridium oxides prior to the beginning of the AST plotted in Figure 3.3c point at a lower extent of oxidation for the as-synthesized sample vs. IrO<sub>2</sub>-HT. Chiefly, this observation agrees well with the differences in OER-activities observed for these materials, since partially-reduced iridium oxides (e.g., IrOOH) have been reported to be more OER-active than their fully oxidized counterparts (i.e., IrO<sub>2</sub>). Beyond these initial differences, though, Figures 3.3a and 3.3b unveil that neither of the catalysts underwent a significant change of its oxidation state in the course of the AST.

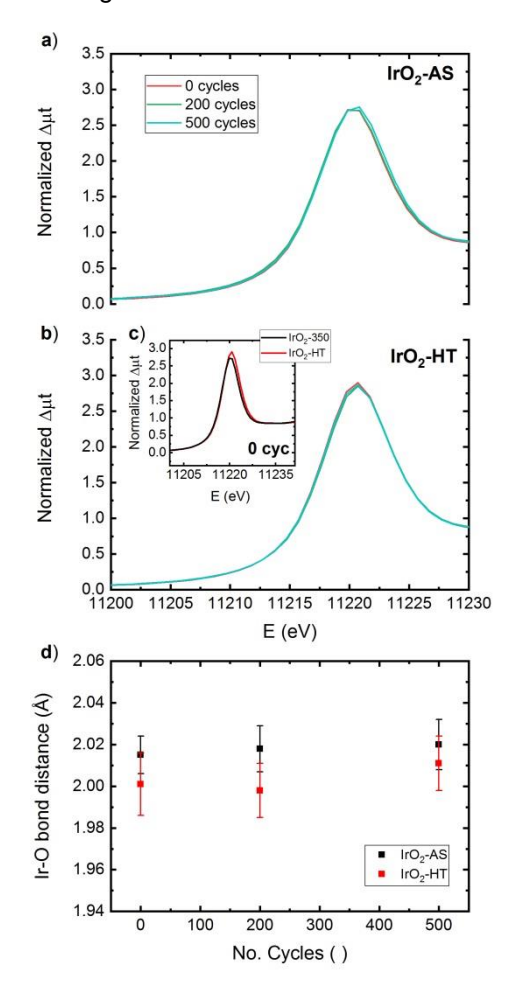


**Figure 3.3.** AST-cycle dependent evolution of the *operando* XANES (recorded at 1.0 V vs. RHE) of the as-synthesized and heat-treated iridium oxides (a vs. b, respectively), along with a comparison of the beginning of life spectra (c). Complementing, cycle-dependent evolution of the Ir-O bonding distance derived from the fitting of the *operando* EXAFS for both catalysts (d).

The above observations regarding the oxides' initial oxidation state and lack of subsequent changes thereof during the AST were mirrored by the catalysts' *operando* EXAFS; specifically, when the normalized and Fourier-transformed spectra were fitted, the derived Ir-O bonding were slightly larger for the IrO<sub>2</sub>-AS sample (see Fig. 3.3d), indicating a lower extent of oxidation for this material [1]. Moreover, these bonding distances also remained unmodified for both catalysts along the AST.



#### 3.3.3 SAXS-derived operando changes in the oxides' morphology

In the absence of changes in the XAS-derived results discussed above, SAXS can discern a possible evolution of the catalysts' morphology in the course of the AST. Thus, Figures 3.4a and 3.4b display the initial and final SAXS curves recorded on both catalysts, and that in the case of the  $IrO_2$ -HT sample do not feature any AST-derived changes (cf. Fig. 3.4b). In the case of the  $IrO_2$ -AS sample, though, a significantly different behaviour is observed, since (in good agreement with its poorer electrochemical stability, cf. Fig. 3.2b) its SAXS curves do change in the course of the AST. In this case, the SAXS data were successfully fitted with a scattering model that considers each  $IrO_x$  particle as a cylinder with a diameter (D) greater than its height (L), in agreement with our TEM observations (not shown). As illustrated in Figure 3.5a, the distribution of the cylinder's diameter becomes narrower and shifts towards larger average values (<D>'s) in the course of the AST. This last observation is well summarized in Fig. 3.5b, which displays the increase of <D> with the cycle number. Notably, the overall AST leads to an increase of  $\approx$  30 % in this parameter. Complementarily, the cylinders' average height (<L>) decreases by  $\approx$  40% (cf. Fig. 3.5c), and thus the AST leads to flattening of the initial cylinders into discs.

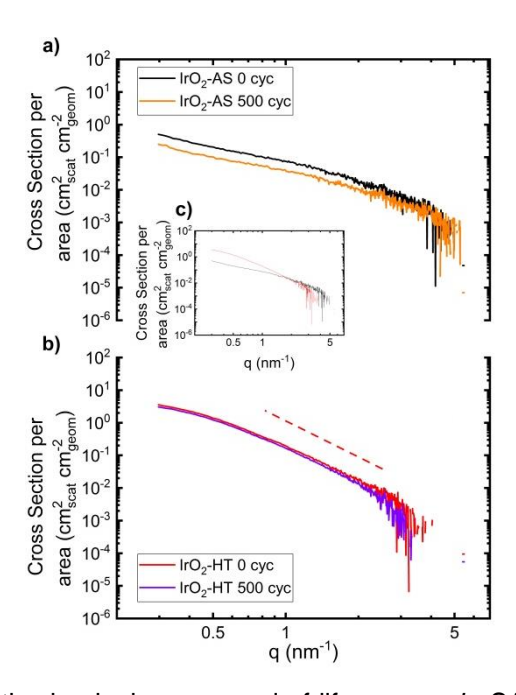


**Figure 3.4.** Comparison of the beginning- vs. end-of-life *operando* SAXS patterns recorded (while holding the potential at 1.0 V vs. RHE) on the IrO<sub>2</sub>-AS or the IrO<sub>2</sub>-HT samples (a vs. b, respectively). Corresponding comparison of the beginning-of-life SAXS for both catalysts (c).



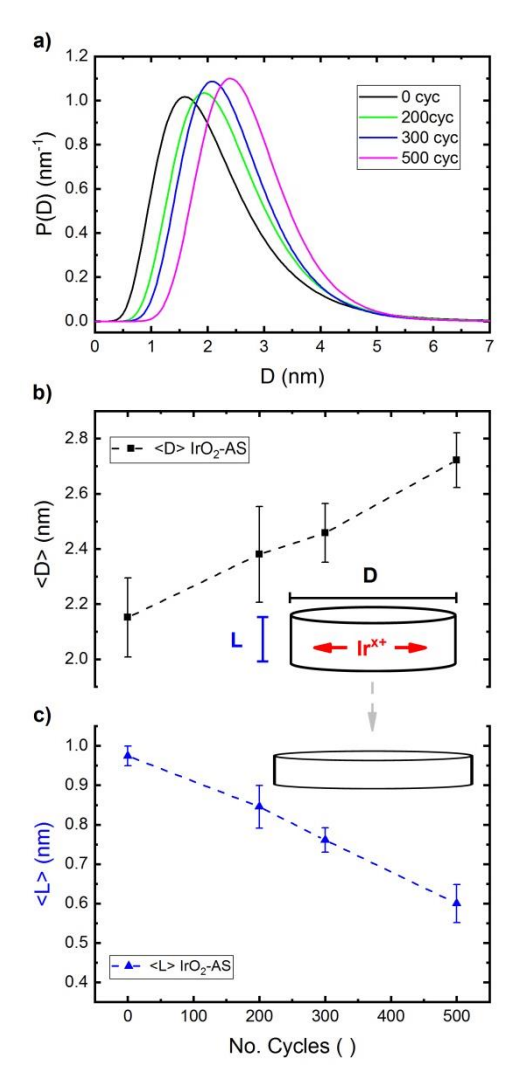


**Figure 3.5.** Operando SAXS-derived, cycle-dependent evolution of the cylinders' diameter log-normal distribution in the course of the electrochemical AST (a). Corresponding changes in the cylinder's average diameter (<D>, b) and height (<L>, c).

## 3.4 Conclusions and outlook

In summary, we succeeded at preparing a high surface area iridium oxide OER-catalyst, as well as a heat treated derivative with a  $\approx$  30 % lower surface area. Whereas the former material displayed a significantly better OER-activity, it also suffered from a poorer cycling stability in an AST that mimics PEM-electrolyzer operation. To understand the reason for these differences among catalysts, we used a combined XAS and SAXS setup available at the SLS that can provide invaluable information about operando changes in a sample's composition and morphology. In this regard, the XAS results showed that the enhanced OER-activity of the IrO<sub>2</sub>-AS sample stems from its lower extent of oxidation when compared to its heat-treated derivative. Nevertheless, no significant changes in the composition of either of the materials during the AST could be inferred from these XAS results. SAXS, on the other hand, confirmed the morphological stability of the IrO<sub>2</sub>-HT catalyst, while disclosing the flattening of the cylindrically shaped particles in IrO<sub>2</sub>-AS. Thus, the loss of OER-activity in the latter material is likely



linked to a decrease of the fractional contribution of more OER-active facets (corresponding to the shortening cylinders' straight edges) to the overall surface area and catalytic process.

## 3.5 References

- [1] U. Babic, M. Suermann, N. B. Felix, L. Gubler, T, J. Schmidt, J. Electrochem. Soc. 164 (2017), F387
- [2] M. Bernt, A. Siebel, H. A. Gasteiger, J. Electrochem. Soc. 165 (2018), F305.
- [3] D. F. Abbott, D. Lebedev, K. Waltar, M. Povia, M. Nachtegaal, E. Fabbri, C. Cope, T. J. Schmidt, *Chem. Mater.* **28** (2016), 6591.
- [4] M. Povia, J. Herranz, T. Binninger, M. Nachtegaal, A. Diaz, J. Kohlbrecher, D. F. Abbott, B. J. Kim, T. J. Schmidt, *ACS Catal.* **8** (2018), 7000.
- [5] T. Binninger, E. Fabbri, A. Patru, M. Garganourakis, J. Han, D. F. Abbott, O. Sereda, R. Kötz, A. Menzel, M. Nachtegaal, T. J. Schmidt, *J. Electrochem. Soc.* **163** (2016), H913.
- [6] D. W. Schaefer, K. D. Keefer, Phys. Rev. Lett. 56 (1986), 2199.